Published in final edited form as:
J Magn Reson Imaging. 2014 November ; 40(5): 1022–1040. doi:10.1002/jmri.24521.

Non-Cartesian Parallel Imaging Reconstruction

Katherine L. Wright, B.S.[1], **Jesse I. Hamilton, B.S.**[1], **Mark A. Griswold, Ph.D.**[1,2], **Vikas Gulani, M.D., Ph.D.**[1,2], and **Nicole Seiberlich, Ph.D.**[1]

[1]Dept. of Biomedical Engineering, Case Western Reserve University, Cleveland, OH

[2]Dept. of Radiology, Case Western Reserve University, Cleveland, Cleveland, OH

Abstract

Non-Cartesian parallel imaging has played an important role in reducing data acquisition time in MRI. The use of non-Cartesian trajectories can enable more efficient coverage of k-space, which can be leveraged to reduce scan times. These trajectories can be undersampled to achieve even faster scan times, but the resulting images may contain aliasing artifacts. Just as Cartesian parallel imaging can be employed to reconstruct images from undersampled Cartesian data, non-Cartesian parallel imaging methods can mitigate aliasing artifacts by using additional spatial encoding information in the form of the non-homogeneous sensitivities of multi-coil phased arrays.

This review will begin with an overview of non-Cartesian k-space trajectories and their sampling properties, followed by an in-depth discussion of several selected non-Cartesian parallel imaging algorithms. Three representative non-Cartesian parallel imaging methods will be described, including Conjugate Gradient SENSE (CG SENSE), non-Cartesian GRAPPA, and Iterative Self-Consistent Parallel Imaging Reconstruction (SPIRiT). After a discussion of these three techniques, several potential promising clinical applications of non-Cartesian parallel imaging will be covered.

Keywords

Non-Cartesian; Parallel Imaging; CG SENSE; SPIRiT; Non-Cartesian GRAPPA

Introduction

MRI is a widely-used medical imaging modality, but long data acquisition times can make the use of MRI challenging for some medical imaging applications. The limiting factor in data acquisition speed is the time needed to play out gradient waveforms. Currently, the maximum gradient strengths and slew rates in modern MRI systems are constrained by physiological considerations. Therefore, imaging speed can only be further improved by increasing the efficiency of gradient waveforms or by reducing the amount of gradient encoding. Non-Cartesian parallel imaging seeks to use both of these approaches simultaneously to significantly reduce the amount of time required to collect MRI data.

Address correspondence to: Nicole Seiberlich, Case Western Reserve University, Room 309, Wickenden Building, 2071 Martin Luther King Jr. Drive, Cleveland, OH, USA 44106-7207, 216-368-6248, nes30@case.edu.

The goal of this review is to discuss the adaptation of parallel imaging methods for the reconstruction of accelerated non-Cartesian data. Parallel imaging techniques have been extensively employed to reduce scan time for Cartesian trajectories, but these methods must be significantly modified to work with data acquired using non-Cartesian trajectories to traverse k-space. While there have been many interesting and valid implementations of non-Cartesian parallel imaging, three representative methods that span the various types of reconstruction classifications will specifically be examined, namely Conjugate Gradient SENSE (CG SENSE) (1), non-Cartesian GRAPPA (2–5), and Iterative Self Consistent Parallel Imaging Reconstruction (SPIRiT) (6). These three methods were selected as they are often used in research settings, and they illustrate important theoretical and practical concepts of non-Cartesian parallel imaging techniques. With an understanding of these methods, many other non-Cartesian parallel imaging approaches not discussed here can be understood as well.

Non-Cartesian K-Space Sampling

Almost all clinical MR imaging is performed by acquiring k-space along a Cartesian, or rectilinear, trajectory. Data are sampled line-by-line on a rectangular grid as shown in Figure 1 (top left). A benefit of this sampling trajectory is that the data are uniformly sampled, and images can be easily and quickly reconstructed using a fast Fourier transform (FFT). However, k-space can also be sampled in an arbitrary non-Cartesian manner, and different sampling trajectories will have different properties and implications for the reconstructed image. Many non-Cartesian trajectories have been explored, including but not limited to radial/projection (7,8), spiral (9,10), rosette (11), BLADE/PROPELLER (12), and stochastic (13) trajectories.

Sampling along a non-Cartesian trajectory can have many benefits based on the unique properties of these trajectories. One of the most important properties of non-Cartesian trajectories is their potential for efficient use of MR gradient hardware and therefore rapid coverage of k-space. Additionally, many non-Cartesian trajectories contain fewer coherent artifacts from undersampling (14) are less affected by motion (8,15), allow image contrast to be updated throughout data acquisition (16), and/or enable motion correction (12), self-navigation (17,18), ultra-short TE acquisitions (19), spectrally selective imaging (11), and chemical shift imaging (20).

While non-Cartesian trajectories have many advantages, it is considerably more difficult to reconstruct images from non-Cartesian data because the non-Cartesian data points do not fall on a grid in k-space. There are many approaches for reconstructing non-Cartesian data (21–27) using a class of methods generally referred to as gridding, which transform non-Cartesian k-space data into either Cartesian k-space data or images. Such gridding operations typically require parameters such as the density compensation function (DCF), which takes the non-uniform sampling density of the data into account, although some iterative gridding methods such as (25) can be performed without a DCF. All non-Cartesian reconstructions performed in this manuscript employed the non-uniform fast Fourier transform (NUFFT) (21), which has been made available in an open-source toolbox (28). Density compensation functions were determined for radial data using the Voronoi method

(29) and for the BLADE dataset using the method by Pipe, et al. (23). Both of these density compensation methods are available open-source in (28). It is also important to note that these reconstruction methods require knowledge of the actual trajectory used to acquire the non-Cartesian data, which may be different than the theoretical trajectory because of hardware imperfections. In order to avoid image artifacts due to differences between the desired and actual trajectories, the trajectory should be measured or approximated prior to image reconstruction (30–32).

In MRI, k-space data are often intentionally undersampled to reduce scan time. If the spacing between k-space points becomes too large, such that the Nyquist criterion is not met, aliasing artifacts can appear. In the Cartesian case, data are undersampled in the phase encoding direction as seen in Figure 1 (bottom left), and the aliasing occurs only along that direction. In the non-Cartesian parallel imaging case, data are undersampled and this form of undersampling relates to the type of trajectory employed. For example, this may involve collecting a subset of projections from a radial trajectory or skipping some arms in a spiral acquisition as seen in Figures 1 (bottom central and bottom right).

When data are undersampled, the ratio of the amount of data in a fully-sampled scan to that in an undersampled scan is defined as the acceleration factor *R*. It is good practice to specify whether the acceleration factor is reported with respect to a fully-sampled Cartesian or non-Cartesian grid. For instance, an image with size 128×128 would require $\frac{\pi}{2}(128) \approx 200$ projections to be completely free of aliasing artifacts; if only 20 projections were acquired, the acceleration with respect to the Nyquist limit would be $R = 10$. However, the acceleration factor with respect to the fully-sampled Cartesian dataset would only be 128/20 ≈ 6.4. Because either or both values could be reported, it is important to specify the metric that is used to determine the acceleration. The aliasing artifacts resulting from undersampled non-Cartesian k-space data depend on the type of trajectory, the amount of data collected, and the density compensation function. The form of the artifacts can be understood by looking at the point spread function (PSF) of the undersampled trajectory. Some examples of aliasing artifacts and PSFs for undersampled Cartesian, radial, and variable density spiral trajectories are shown in Figure 2. The undersampled radial and spiral data were gridded using a DCF suitable for fully-sampled non-Cartesian data, and show significant streak and swirling artifacts due to aliasing. By selecting a DCF which weights high spatial frequencies to a lesser degree, these artifacts can be “converted” to blurring; a detailed treatment of how the choice of DCF affects aliasing artifacts can be found in (33). In general, aliasing artifacts from undersampled non-Cartesian trajectories tend to be more diffuse and less coherent than their Cartesian counterparts because data reduction is not uniform across k-space.

Non-Cartesian Parallel Imaging

As described above, non-Cartesian trajectories can be used to increase acquisition speed by sampling k-space more efficiently, and data acquisition can be further accelerated by undersampling these non-Cartesian trajectories. While low levels of undersampling can often be tolerated (14), the resulting aliasing artifacts from highly undersampled data must be mitigated to achieve clinically acceptable image quality. Parallel imaging algorithms

have been applied to undersampled Cartesian data (34–36) to reduce aliasing artifacts by using the additional spatial information provided by an array of receiver coils. Combining parallel imaging reconstruction algorithms with highly accelerated non-Cartesian trajectories would combine the benefits of both methods, allowing much faster imaging speed than is possible with either method alone.

Non-Cartesian parallel imaging uses the same general approach as Cartesian parallel imaging by taking advantage of additional spatial information from coil sensitivities for the reconstruction of undersampled non-Cartesian data. However, applying these algorithms to undersampled non-Cartesian data is not trivial. As described above, the aliasing is more complicated with trajectories such as radial and spiral due to their complex PSFs,. As will be seen later, this more complex aliasing can complicate SENSE-type reconstructions, and the non-uniform undersampling throughout k-space can complicate GRAPPA-type reconstructions. Thus, traditional parallel imaging techniques must be adapted for use with undersampled non-Cartesian trajectories. The most commonly-used non-Cartesian parallel imaging algorithms are similar to existing Cartesian parallel imaging methods in approach and general properties, and thus a complete review of these basic methods is beneficial to understanding non-Cartesian parallel imaging and can be found in other review papers, including (37–39).

In addition to increased imaging speed, non-Cartesian parallel imaging offers a number of other potential advantages over Cartesian approaches. The g-factor, which describes the noise enhancement resulting from the use of a parallel imaging algorithm, is significantly lower for non-Cartesian trajectories than for Cartesian data at the same data reduction factor (40). The relative retention of SNR is due to the fact that the acceleration is divided between two directions in 2D non-Cartesian imaging, whereas acceleration is performed in one direction (the phase encoding direction) in Cartesian imaging. The division of acceleration among several directions enables the coil sensitivities to be used more effectively. Additionally, because typically employed non-Cartesian trajectories are oversampled in the center of k-space, the full acceleration is only realized at the periphery of k-space. As the high-signal k-space center is completely captured even in undersampled datasets, less noise enhancement is seen in highly accelerated non-Cartesian parallel imaging reconstructions. These factors allow higher data reduction rates to be employed with non-Cartesian trajectories than when using standard Cartesian parallel imaging, warranting the use of more complex non-Cartesian approaches.

Many non-Cartesian parallel imaging algorithms have been proposed, including but not limited to: Conjugate Gradient SENSE (CG SENSE) (1), non-Cartesian GRAPPA (2–5,41,42), iTerative Self Consistent Parallel Imaging Reconstruction (SPIRiT) (6), Partially Parallel Imaging with Localized Sensitivities (PILS) (43,44), parallel imaging for arbitrary trajectories using k-space sparse matrices (kSPA) (45), Parallel MRI with Adaptive Radius in k-Space (PARS) (46,47), and parallel reconstruction Based On Successive Convolution Operations (BOSCO) (48). It is instructive to briefly examine the various types of non-Cartesian parallel imaging algorithms and to categorize them for comparison. Non-Cartesian parallel imaging reconstructions can be performed in the image domain using methods including CG SENSE, SPIRiT, or PILS, or in k-space with non-Cartesian GRAPPA, kSPA,

PARS, or BOSCO. Reconstructions can be performed using direct methods (non-Cartesian GRAPPA, PILS, kSPA, PARS, or BOSCO), or using iterative algorithms (CG SENSE and SPIRiT). Additionally, reconstructions can employ coil sensitivity information (CG SENSE, PILS, kSPA, or PARS) or k-space autocalibration data (non-Cartesian GRAPPA, SPIRiT, and BOSCO). Finally, the result of these reconstruction algorithms can be a reconstructed image (CG SENSE, SPIRiT, and PILS), a Cartesian k-space (SPIRiT, kSPA, and PARS), or a non-Cartesian k-space (non-Cartesian GRAPPA).

While there are many effective reconstruction algorithms, as can be seen above, three representative methods that span the range of reconstruction types have been selected for review in this manuscript, namely CG SENSE (1), non-Cartesian GRAPPA (2–5,42), and SPIRiT (6). Table 1 provides a summary of the manuscript(s) and reconstruction details for these three non-Cartesian parallel imaging methods. CG SENSE works in the image domain using an iterative algorithm and requires coil sensitivity information. Non-Cartesian GRAPPA techniques reconstruct missing data in k-space using a direct reconstruction approach, and require autocalibration data. SPIRiT can be performed in either the image domain or in k-space and uses an iterative algorithm with a self-calibrating approach, although Cartesian calibration data can also be used. In the following sections, the theory behind these methods will be described, and each reconstruction method will be demonstrated on undersampled radial data.

Conjugate Gradient SENSE (CG SENSE)

SENSE-based reconstructions use the additional spatial encoding information from a multi-coil array to reconstruct unaliased images in the image domain. SENSE describes a system of equations that relates the coil sensitivities, gradient encoding, and acquired aliased pixels to a vector of unaliased pixels. If the acceleration factor is less than the number of coils used to acquire the images, this relationship is fully-determined and the unaliased pixels can be reconstructed. For instance, if a data acceleration rate of two is used in a Cartesian scan, aliasing occurs along the phase encoding direction, and two pixels in the image fold together. However, if an eight-channel receiver coil is used to collect the data, there are eight separate estimates for each pixel, which can be used to unfold the two aliased pixels from each other. In this case, despite the data undersampling, each system of equations is over-determined by a factor of four, which allows the reconstruction of unaliased images. Additionally, the more over-determined the system of equations is, the better the reconstruction results will be. The SENSE algorithm can be adapted for use with non-Cartesian data (1,49) and is summarized in-depth below.

Theory and Implementation of CG SENSE—CG SENSE is based on the SENSE algorithm, and is used to unfold aliasing artifacts resulting from undersampled non-Cartesian data using explicit knowledge of coil sensitivity information (35). As mentioned previously, the difficulty in performing non-Cartesian parallel imaging with a SENSE-based reconstruction stems from the complex PSFs of undersampled non-Cartesian data and, therefore, the complicated aliasing that must be unfolded. Theoretically, any of the image pixels can be aliased with any other pixel, which makes the unfolding matrices extremely large, as seen below. While the original mathematical concepts in SENSE still apply to non-

Cartesian data, solving the unfolding problem directly would be extremely computationally intensive. Thus, Pruessmann et al. proposed using the conjugate gradient (CG) algorithm as an iterative approach for the reconstruction. The mathematical basis of this algorithm has been previously described in references (1,39), and is summarized below.

The SENSE formulation uses a system of equations relating the object to be imaged (*v*), the acquired k-space data (*m*), and the encoding matrix which transforms the image to k-space (*E*):

$$Ev=m. \quad [5]$$

The acquired data *m* has size $n_c n_k$, where n_c is the number of coils and n_k is the number of sampled positions in k-space. The reconstructed image vector *v* has size N^2, where N is the matrix size of the image. The encoding matrix *E* accounts for all spatial encoding information from gradients and coil sensitivities, and can be described as a combination of the Fourier terms and sensitivity weighting from the array of coils:

$$E=e^{ik_\kappa r_p}C_l(r_p), \quad [6]$$

where r_p is the p^{th} image pixel, k_κ is the κ^{th} k-space value, and $C_l(r_p)$ is the coil sensitivity of coil *l* at pixel r_p. Note that the encoding matrix *E* is very large with size $n_c n_k \times N^2$.

In order to solve for the reconstructed image *v* in Equation 5, the system of equations must be fully determined, such that $n_c n_k \geq N^2$. If the data are fully-sampled ($n_k \geq N^2$), this relationship is fully-determined, and an image can be generated even when using a single coil for data collection. If *m* is undersampled to accelerate data acquisition and n_k reduced to n_k/R, this system of equations can still be theoretically solved as long as the acceleration factor is less than the number of coils used to acquire the data, such that $n_c n_k/R \geq N^2$. While a solution can be found for *v* if Equation 5 is exactly determined and $n_c n_k/R = N^2$, the solution for *v* will be improved if more data points are acquired and the system of equations is overdetermined.

In order to solve for the reconstructed image using Equation 5, *E* must be inverted, which would be difficult given the size of this matrix. For example, if 64 radial projections are acquired with an eight-channel receiver coil for an image matrix size of 128×128, *E* would be over determined by a factor of four. However, it would have size $(8\times128\times64)\times128^2$, and a large number ($\sim128^6$) of operations would be necessary to directly solve for the image pixels in *v*. This example illustrates why it is infeasible to directly apply the SENSE algorithm to reconstruct undersampled non-Cartesian data. Thus, instead of performing a direct inversion of the encoding matrix as in Cartesian SENSE, CG SENSE incorporates the iterative conjugate gradient algorithm (50) to efficiently solve for the unaliased image. While other iterative algorithms exist for solving large linear systems of equations, the CG approach is attractive because it converges rapidly and does not necessarily require regularization.

To more easily formulate the CG SENSE reconstruction problem, a matrix *F* is introduced to 'undo' the encoding, such that:

$$\mathrm{FE}=\mathrm{Id}, \quad [7]$$

where *F* is the reconstruction matrix and *Id* is the identity matrix. An unaliased image can be found by multiplying both sides of Equation 5 by the *F* matrix, which can be expressed by:

$$\mathrm{v}=\mathrm{Fm}. \quad [8]$$

The reconstruction matrix *F* can be computed by using Equations 6 and 7 and a Moore-Penrose inversion:

$$\mathrm{F}=(\mathrm{E}^{\mathrm{H}}\psi^{-1}\mathrm{E})^{-1}\mathrm{E}^{\mathrm{H}}\psi^{-1}, \quad [9]$$

where ψ is the sampling noise matrix, which can obtained from noise measurement data as described in reference (1). While this formulation gives the reconstruction matrix for the optimal SNR reconstruction, the equations can be simplified by approximating the noise matrix ψ by the identity matrix:

$$\mathrm{F}=(\mathrm{E}^{\mathrm{H}}\mathrm{E})^{-1}\mathrm{E}^{\mathrm{H}}. \quad [10]$$

With this version of the reconstruction matrix, Equation 8 can be rewritten to avoid the computationally inefficient matrix inversion:

$$(\mathrm{E}^{\mathrm{H}}\mathrm{E})\mathrm{v}=\mathrm{E}^{\mathrm{H}}\mathrm{m}. \quad [11]$$

This set of equations can now be solved using CG without the need to explicitly write out or invert the E matrix. Instead, the function of the encoding matrix can be replicated applying the Fourier transform and coil sensitivity matrices (or their inverses). Because the data in the v matrix are non-Cartesian, the FFT cannot be used to transition between k-space and the image domain. Thus, a gridding step or some additional interpolation must be performed so that data are on a Cartesian grid prior to applying the FFT.

The CG SENSE reconstruction process can also be made more efficient by utilizing pre-conditioning. Here, pre-conditioning involves including terms for density and intensity compensation, which offer a better initial estimate of the image to reduce the number of iterations which must be employed. Density compensation is applied by including a matrix *D*, which is a diagonal matrix containing the values of the DCF, to account for differences in the density of the sampling trajectory. Intensity compensation corrects for the sum-of-square weighting that exists due to coil sensitivity variations. A diagonal matrix *I* containing the inverse square-root of the coil weightings (known from the coil maps) is used to compensate for these intensity differences. Including these terms to Equation 11 leads to the following formulation:

$$(\mathrm{IE^H DEI})(\mathrm{I^{-1}v}) = \mathrm{IE^H D\,m}. \quad [12]$$

It is important to note that neither the D nor the I matrix must be employed for the CG SENSE method; these matrices mainly serve to speed the convergence of the algorithm, but CG SENSE can be employed without either or both terms (51).Two final considerations for improving the efficiency of CG SENSE are proper initialization and regularization. An initial guess for *v* must be selected to start the CG algorithm. Fewer iterations are required if *v* is already a good estimate of the final image. One possible initial guess is the gridded undersampled data. If pre-conditioning is performed, an image vector of zeros can also be a good choice. Regularization is not a requirement for the CG SENSE reconstruction and was not utilized in the initial implementation. However, the addition of a regularization term can ensure convergence and improve the speed of convergence (52–56). Different regularization algorithms can be utilized, including Tikhonov, weighted Tikhonov, total variation, or L1-norm wavelet (57–60).

A summary of the CG SENSE algorithm is included below and is depicted in the diagram shown in Figure 3. The following steps are taken to solve for the final reconstructed image vector *v*:

1. The right side of Equation 12 is calculated by taking the acquired k-space data and performing density compensation (if desired), gridding, and the Fourier transform for each coil, multiplying by the complex conjugate of the coil sensitivities, summing the multi-coil images together, and performing intensity correction. The result is an estimate of the reconstructed image.
2. Within the CG algorithm, the reconstructed image from Step 1 is compared to the initial guess image, and a residuum vector is calculated.
3. The residuum vector is used to compute a new estimate of $(\mathrm{I^{-1}v})$, and the left side of Equation 12 is computed with this new estimate by performing intensity correction, multiplying the image by coil sensitivity profiles, applying the Fourier transform to each multi-coil image, and degridding the k-space data.
4. The original acquired k-space data is reinserted into estimated k-space for data consistency, and the right side of Equation 12 is then recalculated using this new k-space data as described in Step 1. The result is a new estimate of the reconstructed image, and the result is fed into the CG algorithm.
5. The accuracy of the current approximation is estimated by calculating the difference between the new estimate and the previous estimate, and Steps 2-4 continue until the stopping criterion is reached where the residuum is less than a pre-determined accuracy measure (ε). This stopping criterion depends on several factors, such as the acceleration factor, trajectory, noise level, coil array used, and implementation of the reconstruction, and it can be determined empirically or analytically (1,52).
6. Once the stopping criterion is reached, intensity correction is applied, yielding the final unaliased image *v*.

CG SENSE has also been implemented and provided in open-source form within the Gadgetron image reconstruction framework (61), the image reconstruction toolbox (used in this work) (28), and through educational online resources (62).

Demonstration of CG SENSE—In order to demonstrate the power of CG SENSE for non-Cartesian parallel imaging, fully-sampled radial data were acquired in an axial slice in the abdomen after administration of a single dose (0.1 mmol/kg) of gadobenate dimeglumine (Multihance, Bracco Diagnostics Inc., Princeton, NJ). The radial data set was acquired during a breath-hold with a matrix size of 192×192 and 200 projections with a FLASH readout a 3T Siemens Skyra (Erlangen, Germany). Acquisition parameters include: repetition time: 2.78ms, echo time: 1.19ms, FoV=350mm^2, bandwidth: 1000 Hz/pixel, fat saturation. Coil maps were calculated for the 16 coils using the adaptive combination method (63).

The original fully-sampled data are reconstructed and shown on the left-hand side of Figure 4 for reference. The data were then retrospectively undersampled by a radial acceleration factor of four, such that 67 of the 200 projections were used. This is equivalent to an acceleration factor 4.5 with respect to the Nyquist criterion. As shown in Figure 4 center-left, the undersampled data were used to generate an image in order to demonstrate the level of aliasing at this acceleration factor.

A fully-sampled image was then reconstructed using the undersampled radial data and the CG SENSE algorithm described above using the implementation available in (28). These data were reconstructed using a zero image for initialization, no regularization, and four iterations. Density compensation weights using the Voronoi method (29) were used for preconditioning of the CG algorithm, and the NUFFT was performed using the image reconstruction toolbox (21,28). As seen in Figure 4 center-right, the radial streaking artifacts and noise amplification have largely been removed by CG SENSE. In order to demonstrate the use of regularization in CG SENSE, the reconstruction was also performed with the same reconstruction parameters described above with the addition of Tikhonov regularization (a regularization parameter of 0.25 was selected empirically). This regularization method is available within the open-source implementation (28). The resulting reconstructed image can be seen in Figure 4 right; note that the regularization term places more emphasis on the original data, resulting in a reconstruction which in this case retains some streak artifacts but appears less blurry than the reconstruction without regularization.

Strengths/Limitations of CG SENSE—CG SENSE has been used in many different applications over the last decade, demonstrating that it is robust and easily applied to different types of data. This algorithm does not require alterations based on the sampling trajectory, which is simply supplied as an input to the algorithm for the gridding process. Additionally, the output of the algorithm is a reconstructed Cartesian image where the coils have been combined. Thus, no additional reconstruction steps, such as a NUFFT or coil combination, are necessary after the parallel imaging algorithm is complete.

While CG SENSE is a commonly-used parallel imaging reconstruction method, it does have some limitations. One challenge when applying CG SENSE is the need for coil sensitivity maps, which are required for all SENSE-based reconstructions. Accurate coil maps can be difficult to obtain in certain applications, which can negatively impact the resulting image quality. For example, it can be difficult to estimate coil sensitivity maps in image areas with low signal, such as the lungs. Accurate coil sensitivity maps are also difficult to acquire in applications where patient motion may occur. In these cases, the actual coils may move after the pre-scan used to collect coil information, altering the coil sensitivity profiles and causing errors in the sensitivity maps. These errors will manifest as residual aliasing artifacts in the reconstructed image.

Another potential limitation of CG SENSE is that the stopping criteria for the iterative reconstruction must be defined by the user. If too few iterations are performed, the reconstructed images will exhibit residual aliasing artifacts. If too many iterations are performed such that the residual vector essentially becomes noise, the algorithm will begin to reconstruct the noise itself, increasing the noise level in the reconstructed image. One way to tackle this challenge would be to output the image after each iteration and identify the “best” reconstruction based on an image quality metric. Selection of the stopping criteria can also be performed using an L-curve analysis (52).

Convergence of the reconstruction and selection of the stopping criteria can also be affected by the use of regularization. For example, Tikhonov regularization can be combined with CG SENSE to reduce noise amplification in reconstructed images (53). The drawback to regularization is that it requires selection of an additional parameter that weights the importance of this constraint in the reconstruction. Determining this regularization parameter can be difficult, and selecting the wrong parameter can also lead to decreased image quality.

Despite minor limitations, CG SENSE has been successfully used in many applications, including cardiac imaging, coronary artery imaging, and functional MRI (1,64,65). Additionally, this reconstruction can be implemented with GPUs to provide fast reconstructions (61,66). Due to the iterative nature of CG SENSE and the ability to combine this technique with additional constraints, CG SENSE has also been implemented in conjunction with other reconstruction approaches, including compressed sensing and spatiotemporal correlations (67–69).

Non-Cartesian GRAPPA

Just as CG SENSE is an extension of SENSE, non-Cartesian GRAPPA is a generalization of GRAPPA (36) for reconstructing images from data acquired along undersampled non-Cartesian trajectories. In this article, the term “non-Cartesian GRAPPA” will refer to a whole collection of methods based on the general GRAPPA approach. In contrast to CG SENSE, non-Cartesian GRAPPA methods are not iterative and do not require prior knowledge of coil sensitivity profiles. Reconstruction is performed directly in k-space by estimating missing data points as weighted linear combinations of known acquired points. The GRAPPA weights implicitly contain information about the coil sensitivity profiles and are determined using one or more fully-sampled training scans. A review of Cartesian

GRAPPA will be presented before discussing how this technique can be adapted for non-Cartesian trajectories.

Theory and Implementation of GRAPPA—In Cartesian GRAPPA, data are collected line-by-line in k-space, and some phase encoding lines are skipped to reduce scan time. Each missing data point, called a target point, is reconstructed by combining a kernel of neighboring acquired points, the source points, with a set of coefficients called GRAPPA weights. In matrix form, the reconstruction is written as:

$$\overrightarrow{S}_{targ} = w \cdot \overrightarrow{S}_{source} \quad [13]$$

where w is the matrix of GRAPPA weights, and $\vec{S}_{targ}$ and $\vec{S}_{source}$ are vectors of target and source points. Both the geometry of the source point kernel and the GRAPPA weights are shift invariant, which means that they can be applied throughout the undersampled k-space (Figure 5 left).

Cartesian GRAPPA is said to be autocalibrating because the GRAPPA weights are estimated using a fully-sampled, low spatial resolution dataset called the autocalibration signal or ACS. Because many sets of both source and target points are known within the ACS, a least squares estimate of the GRAPPA weights can be obtained by a pseudoinverse operation:

$$\hat{w} = \mathrm{pinv}\,(S_{source}) \cdot S_{targ} \quad [14]$$

The source point matrix has a size $n_{rep} \times n_k n_c$, where n_{rep} is the number of kernel occurrences over k-space, n_c is the number of coils, and n_k is the size of the kernel. The target matrix has a size $n_{rep} \times n_k n_c$, making the weight set a matrix of $n_k n_c \times n_c$. This calibration equation is fully-determined when $n_k n_c \geq n_{rep}$. However, when the calibration equation is exactly determined or only slightly overdetermined, the GRAPPA weights can be influenced by noise and the resulting image can contain residual aliasing artifacts. To obtain a better estimate of the GRAPPA weights which is less affected by noise, it is preferable for the calibration equation to be highly overdetermined. Thus the number of kernel repetitions is generally much larger than the theoretical minimum for Cartesian GRAPPA.

Theory and Implementation of Non-Cartesian GRAPPA—Several modifications must be made to GRAPPA in order to reconstruct undersampled non-Cartesian data. Whereas Cartesian sampling is uniform, non-Cartesian trajectories vary in the degree and direction of undersampling across k-space. Different regions of k-space have differently shaped GRAPPA kernels, so they no longer share the same GRAPPA weights (Figure 5 right). Each data point in a radial trajectory, for instance, will have a unique geometry of source and target points in the GRAPPA kernel. This leads to two challenges. First, a large number of GRAPPA weights must be determined, theoretically one for each target point. Second, there is no clear way to calibrate these GRAPPA weights, as each geometry appears only once even in a fully-sampled non-Cartesian dataset.

The first implementation of GRAPPA for the radial trajectory resolved the calibration problem by collecting a fully-sampled non-Cartesian dataset and dividing the k-space into segments (2). Each segment is approximated as a small Cartesian grid that has its own set of GRAPPA weights (Figure 6). Segments are selected to be large enough so there are sufficient occurrences of the GRAPPA kernel to compute a stable estimate of the GRAPPA weights for that particular area of k-space. Radial GRAPPA can only practically be used for dynamic imaging since the calibration scan is already fully-sampled.

One disadvantage of the original non-Cartesian GRAPPA is that the reconstruction must be formulated carefully for different non-Cartesian trajectories, depending on the symmetry of the trajectory. Two techniques for non-Cartesian GRAPPA reconstruction of spiral trajectories which are similar to the radial approach were introduced by Heberlein, et al. (47) and Heidemann, et al (3). Other similar formulations have been described for 1D non-Cartesian data (71) and zig-zag trajectories (72), and can in theory be developed for any trajectory with an axis of symmetry. GRAPPA can be more easily used with BLADE/PROPELLER trajectories, as these types of trajectories contain large patches of Cartesian data which can be reconstructed using Cartesian GRAPPA. However, the GRAPPA weights for PROPELLER data can also be rotated (73), thereby reducing the amount of calibration data required.

One difficulty with the non-Cartesian GRAPPA methods described thus far is the choice of segment size. Typically, large k-space segments are chosen to yield enough kernel repetitions to ensure that the calibration equations are overdetermined. However, segments that are too large can no longer be approximated as Cartesian, and the local GRAPPA weights determined using such a segment will be inaccurate. On the other hand, if the segment is too small, the number of kernel occurrences will also be small, and the calibration equation may not be fully determined. Weight sets may be overly influenced by noise in this situation, and there is danger of overfitting or “copying” calibration data into the reconstructed images.

Through-time non-Cartesian GRAPPA introduced an improved calibration scheme to deal with the challenge of segment size selection (4,5). Compared to previous algorithms where k-space is divided into a few large segments, through-time non-Cartesian GRAPPA uses very small segments or no segmentation at all. In order to obtain the numerous repetitions of the kernels needed to determine the GRAPPA weights, multiple fully-sampled frames of non-Cartesian data are acquired during a pre-scan or post-scan. Rather than moving the kernel through a region of k-space to accumulate instances of known source and target points, the kernel is moved through time (Figure 7 left). Because each target point has a unique kernel geometry that is exactly repeated in every frame of the calibration dataset, this calibration strategy leads to a more robust estimate of the weights.

A summary of non-Cartesian GRAPPA reconstruction is given below and depicted in Figure 7.

1. Collect one or more fully-sampled non-Cartesian datasets for calibration and an undersampled non-Cartesian dataset to be reconstructed

2. Repeat the following steps at each unacquired location in the undersampled k-space:
    a. Locate nearby acquired data points to use as source points in a local GRAPPA kernel
    b. Accumulate occurrences of the non-Cartesian GRAPPA kernel in the calibration dataset using any of several options, including k-space segmentation and through-time calibration
    c. Obtain a least squares estimate of the non-Cartesian GRAPPA weights for a particular location in k-space using Equation 14
    d. Multiply source points in the undersampled data by the local GRAPPA weights from step 2c to reconstruct a given target point

Code for the through-time radial GRAPPA method has been made available in an open-source format: http://www.ismrm.org/mri_unbound/sequence.htm.

Demonstration of the non-Cartesian GRAPPA—To demonstrate the use of non-Cartesian GRAPPA, free-breathing, non-EKG gated cardiac datasets were acquired along a 2D radial TrueFISP trajectory on a 3T Siemens Skyra with following scan parameters: 128×128 image size, 30 receiver channels, repetition time: 2.94ms, echo time: 1.47ms, FoV 300mm^2, and spatial resolution 2.3×2.3×8mm^3. A fully-sampled calibration scan was acquired with 144 projections and 20 frames (scan time 8.5s). A separate fully-sampled scan was performed with 144 projections and retrospectively undersampled to 16 projections (acceleration factor R=12.6 with respect to Nyquist).

Two radial GRAPPA algorithms are demonstrated for comparison (Figure 8). First, the original implementation of radial GRAPPA was performed using a single fully-sampled frame from the calibration scan and a k-space segment spanning 64 readout points and 10 projections. Second, through-time radial GRAPPA was performed using all 20 frames from the calibration scan and a k-space segment spanning 8 readout points and 4 projections. These reconstruction parameters were chosen so that the number of kernel occurrences at each location in k-space would be the same for both non-Cartesian GRAPPA implementations. After reconstruction, the k-space data were density compensated using the Voronoi method (29) and converted to individual coil images using the NUFFT. For comparison, the undersampled data were directly gridded to the image domain to show the extent of aliasing artifacts present in the original data.

Compared to the fully-sampled reference image, the directly gridded image shows severe radial streaking artifacts that are largely removed by both radial GRAPPA reconstructions. The image reconstructed by radial GRAPPA using a large segment size and a single calibration frame still contains some residual aliasing and is slightly blurred. The segment size was not optimized and may not yield the best image quality for this particular dataset. In comparison, the image reconstructed by through-time radial GRAPPA is less corrupted by residual aliasing and appears sharper.

Strengths/Limitations of Non-Cartesian GRAPPA—Non-Cartesian GRAPPA methods have several beneficial properties. They are not iterative, do not use view-sharing or temporal filtering, and do employ model-fitting or make prior assumptions about the data. For a given data reduction factor, the g-factors for non-Cartesian GRAPPA are generally lower than for the Cartesian case (40). However, non-Cartesian GRAPPA implementations that divide k-space into large segments cannot resolve aliasing artifacts when the acceleration factor is high. It is also difficult to choose a proper segment size that yields acceptable image quality. Segments that are too large can result in blurring, while segments that are too small may cause noise enhancement. Additionally, unlike CG SENSE, non-Cartesian GRAPPA techniques must be formulated carefully to accommodate different sampling trajectories.

Through-time Non-Cartesian GRAPPA builds on previous methods with an improved calibration scheme which removes the need for large calibration segments. Like CG SENSE, it has been implemented for online, real-time reconstruction using GPUs and distributed programming (74). Through-time calibration gives a more accurate estimate of GRAPPA weights than previous approaches that divide k-space into large segments. Furthermore, it can work with any trajectory; the reconstruction algorithm will simply need to be adjusted to select the best source points for a given target point.

One drawback of non-Cartesian GRAPPA is the need for at least one, if not several, fully-sampled training scans. However, the calibration can be performed even when the underlying object is moving. For example, calibration for real-time cardiac imaging can be acquired under free-breathing, non-gated conditions without degrading the reconstruction (4). Nevertheless, there may be certain applications where the calibration scan is prohibitive, and a self-calibrating method may be preferred at the cost of a slightly less accurate reconstruction. For example, undersampled data may be acquired along interleaved trajectories that are then merged in a sliding window manner to form a calibration dataset with reduced temporal bandwidth (75,76). There are also methods that synthesize a full calibration dataset from only the Nyquist sampled region at the center of k-space (77) or that interpolate GRAPPA weights directly from undersampled data (78).

Non-Cartesian GRAPPA reconstructions can also be improved by using a specific sampling pattern that modifies aliasing artifacts known as CAIPIRINHA (79,80). While this was originally demonstrated with Cartesian data (79), this technique has been combined with radial GRAPPA to achieve higher acceleration factors in multi-slice acquisitions (80).

SPIRiT

SPIRiT (Iterative Self-Consistent Parallel Imaging Reconstruction) (6) is a parallel imaging method that can be applied to any trajectory, including non-Cartesian sampling patterns, and has many similarities to both CG SENSE and non-Cartesian GRAPPA. SPIRiT relies on two forms of consistency, namely data consistency and calibration consistency, and the SPIRiT reconstruction is framed as a nonlinear optimization which can be solved by a variety of methods. It also has the attractive property that the output is always a Cartesian k-space or a Cartesian image, even though the undersampled data may be non-Cartesian.

Theory of SPIRiT—SPIRiT reconstructs missing data by balancing two key constraints: calibration consistency and data consistency (Figure 9). Calibration consistency is based on the concept that each data point in k-space is correlated with nearby points through the coil sensitivities. Whereas GRAPPA exploits this relationship to reconstruct missing target points from acquired source points, SPIRiT generalizes this notion further. In SPIRiT, each output data point in Cartesian k-space ideally can be expressed as a linear combination of neighboring Cartesian source points over all coils. Mathematically, calibration consistency is expressed as:

$$x = Gx \quad [15]$$

where *x* is a vector containing all Cartesian grid points from every coil and *G* is matrix of coefficients, known as SPIRiT weights. One important distinction from the GRAPPA kernel is that source points in SPIRiT include data that are synthesized during reconstruction and not originally acquired.

As with Cartesian GRAPPA, the SPIRiT kernel is shift invariant and applies the same weights over all of k-space. The SPIRiT weights are determined by accumulating kernel occurrences within a fully-sampled Cartesian region of k-space, which is the ACS data for SPIRiT. There are several options for acquiring calibration data. A small, Nyquist-sampled Cartesian region may be collected together with the undersampled data or as a separate scan. Another alternative is a self-calibrating approach where the densely sampled center of an accelerated non-Cartesian trajectory is interpolated onto a rectangular grid.

Besides calibration consistency, the second key idea of SPIRiT is to ensure that the reconstructed data agree with the raw undersampled data collected at the scanner. This constraint is expressed as:

$$y = Dx \quad [16]$$

where *D* is an operator that transforms reconstructed Cartesian data values *x* to k-space points *y* along the accelerated trajectory. When reconstructed Cartesian k-space data are transformed back onto the undersampled trajectory using inverse gridding, the resulting values should match the original raw data, provided the reconstruction is accurate. When the undersampled trajectory is non-Cartesian, then *D* interpolates Cartesian data points onto a non-uniform grid and can be implemented as convolution gridding (24).

Both calibration consistency and data consistency can be solved simultaneously as a constrained optimization problem:

$$\begin{aligned} &minimize \|(G-I)x\|^2 \\ &Such\ that \|y-Dx\|^2 < \varepsilon \end{aligned} \quad [17]$$

or, equivalently, in an unconstrained Lagrangian form:

$$\arg\min \|y - Dx\|^2 + \lambda \|(G - I)x\|^2 + \sum_i \alpha_i R_i(x) \quad [18]$$

The parameter λ controls the balance between the two consistency constraints, where larger values more heavily enforce calibration consistency and smaller values favor data consistency. A value for λ that yields acceptable image quality can be chosen empirically or analytically.

SPIRiT is flexible in that additional constraints $R_i(x)$ can be applied to the reconstructed data. For example, many medical images are sparse (i.e. the majority of data values are zero) after applying a mathematical transform, such as a discrete wavelet transform (81,82). SPIRiT can be formulated to favor solutions that also are sparse in a particular transform domain. This type of constraint is enforced by minimizing the L1-norm of the data in the transform domain. Another optional constraint is Tikhonov regularization to obtain a reconstruction which is less influenced by noise.

There are several iterative methods available for solving the SPIRiT optimization. Projection over convex sets (POCS) finds a solution that leaves the acquired data untouched, but image quality can be degraded if too many or too few iterations are used. Conjugate gradient descent is also well-suited to numerically solve the optimization since the gradient of the objective function is known analytically

$$\Delta_x = 2D^*(Dx - y) + 2\lambda(G - I)^*(G - I)x \quad [19]$$

and the estimated solution is guaranteed to improve with each iteration.

Implementation of SPIRiT—SPIRiT reconstruction can be performed either directly in k-space or in the image domain, and both approaches are depicted together in Figure 10. Although the overall workflow for both techniques is similar, each has unique benefits and drawbacks. The following discussion assumes that the accelerated scan uses an undersampled non-Cartesian trajectory.

The k-space approach can be summarized in the following steps:

1. The algorithm is initialized with an estimate of the reconstructed Cartesian k-space, *x*. One simple initialization is to directly grid the undersampled non-Cartesian data onto a uniform grid.
2. With each iteration of CG descent, the following steps are performed
    a. To enforce data consistency, the gridding operator *D* interpolates the reconstructed Cartesian k-space data onto the undersampled non-Cartesian trajectory. The difference between the resulting values and the acquired undersampled data is $y - Dx$. This error metric is then gridded back to Cartesian k-space using the adjoint of the gridding operator, giving $D^*(y - Dx)$.

b. To enforce calibration consistency, the operator G convolves the synthesized Cartesian data with a kernel containing the SPIRiT weights. The synthesized Cartesian k-space is subtracted from the result of this convolution, which yields $(G - I)x$.

c. The operator G^* convolves the result of step 2b with flipped and reordered SPIRiT weights. The output of this step is $(G^* - I)(G - I)x$.

d. The result from step 2c is weighted by λ, which controls the tradeoff between data consistency and calibration consistency.

e. The data consistency error from step 2a and the calibration consistency term from step 2d are added together. Their sum is the gradient of the objective function, shown in Equation 19. This value is run through CG descent, which returns an improved estimate of the reconstructed Cartesian k-space.

3. Step 2 is repeated until a suitable stopping criterion is reached. The final result is a fully-sampled Cartesian k-space.

From a practical standpoint, the interpolation kernel and SPIRiT kernel convolutions may be computationally expensive to implement in k-space. One alternative is to perform SPIRiT reconstruction using an image domain approach. The previously outlined steps can still be followed with some modifications:

- The variable x now represents the reconstructed coil images and not the reconstructed Cartesian k-space.
- The algorithm is initialized with an estimate of the uncombined coil images.
- The operator D now performs a NUFFT on the reconstructed coil images to obtain non-Cartesian k-space data, and D^* transforms undersampled non-Cartesian data to their corresponding coil images.
- The operator G multiples coil images by the inverse FFT of the SPIRiT weights in the image domain, and G^* multiplies coil images by the inverse FFT of the flipped and reordered SPIRiT weights.

In the original manuscript, open-source code was made available for SPIRiT and can be found at: http://www.eecs.berkeley.edu/∼mlustig/Software.html(6).

Demonstration of SPIRiT—To demonstrate the capabilities of SPIRiT, a brain scan using a T1-weighted BLADE acquisition was conducted on a 3T Siemens Skyra with the following parameters: 256×256 image matrix, 30 receiver coils, repetition time: 2000ms, echo time: 44ms, FoV 220mm^2, and spatial resolution 0.9×0.9×4mm^3. The fully-sampled data were made up of 44 blades with 9 lines per blade. These data were retrospectively undersampled such that each blade contained only 3 lines (lines 1, 5, and 9), yielding an undersampling factor of R=4 within the blade. The undersampling factor with respect to a Cartesian acquisition was approximately R=1.9 (132 total k-space lines for a 256 matrix). SPIRiT weights were calibrated by gridding the fully-sampled BLADE data to Cartesian k-space and using the center 30×30 region. The image domain approach was used as described

above with a 7×7 SPIRiT kernel and Tikhonov regularization. To initialize the reconstruction, density compensation was applied to the undersampled BLADE k-space data using the DCF proposed by Pipe, et al. (23) before gridding to the image domain. The data consistency and calibration consistency terms were weighted by setting $\lambda = 10$ in Equation 18, and conjugate gradient descent was run with 75 iterations.

Representative results from a single slice are shown in Figure 11. The image reconstructed by directly gridding the undersampled data (center) is corrupted by radial streaking artifacts and blurring when compared to the reference image (left); however, many of these artifacts are removed after SPIRiT reconstruction (right). In this review, the SPIRiT reconstruction parameters were chosen empirically, although it is also possible to do a more rigorous optimization (for example, using L-curve analysis).

Strengths/Limitations—One major advantage of the SPIRiT framework is its flexibility. Like CG SENSE, SPIRiT works with data sampled along arbitrary k-space trajectories, and the output is always a Cartesian k-space or a Cartesian image, which does not require an additional gridding step. SPIRiT also uses the encoding information provided by multiple receiver channels efficiently. It enforces consistency with both calibration data and the raw undersampled data over all of k-space, whereas non-Cartesian GRAPPA only imposes consistency with the calibration data. SPIRiT also has the ability to remove noise from reconstructed data using explicit regularization. Because the SPIRiT kernel spreads information over a small area of k-space with each convolution, this has the effect of locally averaging the data and removing noise after several iterations. Another advantage is the ease of incorporating additional constraints. Some examples include regularization or L1-minimization of the data in a transform domain, which can be useful for removing noise while preserving useful image content. Nevertheless, the flexibility of SPIRiT can lead to potential difficulties. It may not be obvious how to choose appropriate parameter values for the optimization, which may have to be done empirically. An additional consideration is deciding when to terminate the conjugate gradient descent, since SPIRiT may begin to fit noise into the reconstructed images if too many iterations are used.

SPIRiT is relatively expensive computationally. In the k-space domain reconstruction, the interpolation kernel and SPIRiT kernel convolutions may be costly to implement if large kernel sizes are used. With the image domain reconstruction, multiplication by the inverse FFT of the SPIRiT kernel is fast even for large kernel sizes, but there is the additional burden of calculating the NUFFT each iteration. Computational complexity, however, is not a permanent barrier. ESPIRiT is an efficient implementation of SPIRiT with L1-minimization in the wavelet domain that performs an eigenvector decomposition of the SPIRiT operator matrix (83). Clinically realistic runtimes of SPIRiT have been achieved by using multiple GPUs and parallel computing (82).

Combined Cartesian/Non-Cartesian Methods

By using hybrid Cartesian / non-Cartesian 3D trajectories such as the stack-of-stars or stack-of-spirals trajectories (Figure 12 left), data undersampling can potentially be performed in all three spatial directions. While these trajectories are non-Cartesian in the k_x-k_y plane

(usually radial or spiral), Cartesian encoding is performed along k_z. One option for undersampling is to skip k_z encoding lines as shown in Figure 12 center left, and to reconstruct the missing Cartesian data with standard Cartesian parallel imaging techniques (84–86). While this type of reconstruction greatly simplifies the process, acceleration is limited as it would be in standard Cartesian scanning. Another option is to accelerate the data in only the non-Cartesian direction (Figure 12 center right). When this approach is used, the 3D data can be reconstructed using one of the non-Cartesian parallel imaging methods described above. Often a Fourier transform is first applied in the fully-sampled Cartesian k_z direction, which transforms the reconstruction from one large 3D problem to many smaller 2D problems. The reconstruction is often significantly faster, although there can be discontinuities between the 2D slices if iterative methods are employed.

Another potential 3D hybrid trajectory is that used in CAPR (87–90). Here, the read-out is Cartesian along the k_z direction, and the phase encoding positions usually lie along radial projections in the k_x-k_y plane. Data are undersampled by using fewer phase encoding steps, which effectively leads to radial undersampling. Reconstruction can be performed using a non-Cartesian reconstruction technique as described above.

To realize the full acceleration potential of 3D stack-of-stars or stack-of-spirals trajectories, data must be undersampled in both the Cartesian and non-Cartesian directions (Figure 12 right). Again, any of the above-mentioned methods can be used, but the reconstruction problem must be formulated in three-dimensions. For this reason, these types of trajectories are usually reconstructed using GRAPPA-type techniques, although iterative methods can be used. Full 3D non-Cartesian trajectories such as the 3D radial or cones trajectories can also be employed with non-Cartesian parallel imaging, although CG SENSE type reconstructions are usually preferred for these types of data due to the difficulty generating the large number of necessary non-Cartesian GRAPPA weights.

Potential Clinical Applications

Non-Cartesian parallel imaging is primarily used in applications which require a reduced acquisition time. A shortened scan time can be used to image rapidly moving anatomy or changing dynamics. Additionally, by shortening each individual scan, the total MRI exam duration can be decreased, which can help improve patient compliance/comfort and decrease exam costs (91).While non-Cartesian parallel imaging may be advantageous for general MRI scanning, the most intriguing potential clinical applications are those that are only possible with the use of very short acquisition times. Some examples of these applications are discussed below, including cardiac MRI (CMR), MR Angiography (MRA), functional MRI (fMRI), and Dynamic Contrast Enhanced (DCE) MRI.

While non-Cartesian parallel imaging could potentially enable more rapid scanning in clinical settings, these reconstruction algorithms are not commonly used outside of a research setting. There are several reasons for the lack of adoption of non-Cartesian parallel imaging methods. The first is that most clinical scans are performed with Cartesian acquisitions, due to the ease of reconstruction both with and without parallel imaging. With the adoption of non-Cartesian trajectories by major scanner manufacturers, non-Cartesian

parallel imaging may become more important. The second factor is the long reconstruction times and potential need for calibration data. Because any increase in scan time or delays between acquisition and reconstruction are clinically undesirable, these factors must be mitigated before non-Cartesian parallel imaging can be widely adopted. However, self-calibrating methods and rapid reconstructions using platforms including Gadgetron (61) or GPUs (74,82,92) have accelerated both the data collection and image reconstruction times. The final hurdle is the perceived lack of robustness and low acceleration factors which can be achieved using non-Cartesian parallel imaging. However, given recent advances in these algorithms, the potential for significantly faster scanning using non-Cartesian parallel imaging may lead to clinical implementation of these techniques.

Nevertheless, there are a number of applications which could benefit from non-Cartesian parallel imaging. Cardiac MRI is particularly difficult due to cardiac and respiratory motion. Traditional methods for making images of the beating heart use EKG gating to acquire data in a segmented fashion. In order to make images during each phase of the cardiac cycle, data must be acquired over several heartbeats and a constant heart rate must be maintained. Additionally, respiratory motion is an important consideration in cardiac MRI, and the patient must hold his/her breath while the data are collected. However, with the advent of non-Cartesian parallel imaging, real-time cardiac imaging can now be performed by using acquisition times short enough to freeze cardiac and respiratory motion (4,5,93–100). Myocardial perfusion is another difficult exam that could be improved by non-Cartesian parallel imaging (68,69).

Another interesting application of non-Cartesian parallel imaging is for the acquisition of MRA data. In MRA, high spatial resolutions are required to visualize small arteries, and high temporal resolutions are required to capture images during arterial enhancement phases before contrast reaches the veins. Thus, the high spatiotemporal resolutions afforded by using highly accelerated data collection followed by a non-Cartesian parallel imaging reconstruction can be beneficial in many applications including coronary MRAs (86,101,102), peripheral MRAs (87–90), and intracranial MRAs (89,103).

Non-Cartesian parallel imaging can also be valuable in the acquisition of fMRI data. fMRI methods measure changing Blood-Oxygen-Level-Dependent (BOLD) contrast to evaluate neuronal activity. These acquisitions sample data with a high temporal resolution to capture changes in the BOLD response, and they typically use an echo planar imaging (EPI) readout. However, previous works have shown that non-Cartesian trajectories can be used to increase sensitivity to BOLD contrast (104). fMRI acquisitions can also be implemented with non-Cartesian parallel imaging to achieve improved image quality, resolution, and volumetric coverage (64,105,106).

Dynamic Contrast Enhanced (DCE) MRI is another application where temporal resolution requirements can be challenging to meet. In DCE MRI, time-resolved images are acquired with a high temporal resolution to capture changes in signal intensity that are related to changing concentration of gadolinium-based contrast agents. A pharmacokinetic model of the contrast agent is used to quantify perfusion, permeability, and other physiological parameters. Non-Cartesian parallel imaging can achieve the necessary high temporal

resolutions while maintaining clinically relevant spatial resolutions and volumetric coverage, as demonstrated in several applications (107–109).

Conclusion

This review describes how non-Cartesian parallel imaging can be used to reduce MRI data acquisition times. Non-Cartesian sampling of k-space has many advantages, including improved gradient efficiency that allows for faster k-space coverage and the opportunity to collect the center of k-space with every line of data. These non-Cartesian trajectories can be undersampled to further reduce acquisition times and reconstructed with specialized parallel imaging algorithms. The combination of non-Cartesian trajectories and parallel imaging reconstructions allow for larger accelerations and faster scan time than either technique individually, which opens new opportunities for higher spatial and temporal resolutions in many clinical applications.

Acknowledgments

Funding Sources: Case Western Reserve University/Cleveland Clinic CTSC UL1 RR024989, NIH Multidisciplinary KL2RR024990, NHLBI 1 R01HL094557, R00EB011527, 1R01DK098503, NIH Interdisciplinary Biomedical Imaging Training Program T32EB007509.

References

1. Pruessmann KP, Weiger M, Börnert P, Boesiger P. Advances in sensitivity encoding with arbitrary k-space trajectories. Magn Reson Med. 2001; 46(4):638–51. [PubMed: 11590639]
2. Griswold, M.; Heidemann, R.; Jakob, P. Direct parallel imaging reconstruction of radially sampled data using GRAPPA with relative shifts; Proc of the 11th Annual Meeting of the Int Soc Magn Reson Med; Toronto, Canada. 2003; p. 2349
3. Heidemann RM, Griswold MA, Seiberlich N, Krüger G, Kannengiesser SAR, Kiefer B, Wiggins G, Wald LL, Jakob PM. Direct parallel image reconstructions for spiral trajectories using GRAPPA. Magn Reson Med. 2006; 56(2):317–26. [PubMed: 16826608]
4. Seiberlich N, Lee G, Ehses P, Duerk JL, Gilkeson R, Griswold M. Improved temporal resolution in cardiac imaging using through-time spiral GRAPPA. Magn Reson Med. 2011; 66(6):1682–1688. [PubMed: 21523823]
5. Seiberlich N, Ehses P, Duerk J, Gilkeson R, Griswold M. Improved radial GRAPPA calibration for real-time free-breathing cardiac imaging. Magn Reson Med. 2011; 65(2):492–505. [PubMed: 20872865]
6. Lustig M, Pauly JM. SPIRiT: Iterative self-consistent parallel imaging reconstruction from arbitrary k-space. Magn Reson Med. 2010; 64(2):457–71. [PubMed: 20665790]
7. Lauterbur P. Image formation by induced local interactions: examples employing nuclear magnetic resonance. Nature. 1973; 242:190–191.
8. Glover GH, Pauly JM. Projection reconstruction techniques for reduction of motion effects in MRI. Magn Reson Med. 1992; 28(2):275–89. [PubMed: 1461126]
9. Ahn CB, Kim JH, Cho ZH. High-speed spiral-scan echo planar NMR imaging-I. IEEE Trans Med Imaging. 1986; 5(1):2–7. [PubMed: 18243976]
10. Meyer CH, Hu BS, Nishimura DG, Macovski A. Fast spiral coronary artery imaging. Magn Reson Med. 1992; 28(2):202–13. [PubMed: 1461123]
11. Noll DC. Multishot rosette trajectories for spectrally selective MR imaging. IEEE Trans Med Imaging. 1997; 16(4):372–7. [PubMed: 9262995]
12. Pipe JG. Motion correction with PROPELLER MRI: application to head motion and free-breathing cardiac imaging. Magn Reson Med. 1999; 42(5):963–9. [PubMed: 10542356]

13. Scheffler K, Hennig J. Frequency resolved single-shot MR imaging using stochastic k-space trajectories. Magn Reson Med. 1996; 35(4):569–76. [PubMed: 8992208]
14. Peters DC, Rohatgi P, Botnar RM, Yeon SB, Kissinger KV, Manning WJ. Characterizing radial undersampling artifacts for cardiac applications. Magn Reson Med. 2006; 55(2):396–403. [PubMed: 16408266]
15. Liao JR, Pauly JM, Brosnan TJ, Pelc NJ. Reduction of motion artifacts in cine MRI using variable-density spiral trajectories. Magn Reson Med. 1997; 37(4):569–75. [PubMed: 9094079]
16. Winkelmann S, Schaeffter T, Koehler T, Eggers H, Doessel O. An optimal radial profile order based on the Golden Ratio for time-resolved MRI. IEEE Trans Med Imaging. 2007; 26(1):68–76. [PubMed: 17243585]
17. Liu C, Bammer R, Kim DH, Moseley ME. Self-navigated interleaved spiral (SNAILS): application to high-resolution diffusion tensor imaging. Magn Reson Med. 2004; 52(6):1388–96. [PubMed: 15562493]
18. Larson AC, White RD, Laub G, McVeigh ER, Li D, Simonetti OP. Self-gated cardiac cine MRI. Magn Reson Med. 2004; 51(1):93–102. [PubMed: 14705049]
19. Qian Y, Boada FE. Acquisition-weighted stack of spirals for fast high-resolution three-dimensional ultra-short echo time MR imaging. Magn Reson Med. 2008; 60(1):135–45. [PubMed: 18581326]
20. Adalsteinsson E, Star-Lack J, Meyer CH, Spielman DM. Reduced spatial side lobes in chemical-shift imaging. Magn Reson Med. 1999; 42(2):314–23. [PubMed: 10440957]
21. Fessler J, Sutton B. Nonuniform fast Fourier transforms using min-max interpolation. IEEE Trans Signal Process. 2003; 51(2):560–574.
22. Rosenfeld D. New approach to gridding using regularization and estimation theory. Magn Reson Med. 2002; 48(1):193–202. [PubMed: 12111946]
23. Pipe JG, Menon P. Sampling density compensation in MRI: rationale and an iterative numerical solution. Magn Reson Med. 1999; 41(1):179–86. [PubMed: 10025627]
24. Jackson J, Meyer C, Nishimura D, Macovski A. Selection of a convolution function for Fourier inversion using gridding. IEEE Trans Med Imaging. 1991; 10(3):473–78. [PubMed: 18222850]
25. Moriguchi H, Duerk JL. Iterative Next-Neighbor Regridding (INNG): improved reconstruction from nonuniformly sampled k-space data using rescaled matrices. Magn Reson Med. 2004; 51(2): 343–52. [PubMed: 14755660]
26. Gabr RE, Aksit P, Bottomley Pa, Youssef ABM, Kadah YM. Deconvolution-interpolation gridding (DING): accurate reconstruction for arbitrary k-space trajectories. Magn Reson Med. 2006; 56(6): 1182–91. [PubMed: 17089380]
27. Rosenfeld D. An optimal and efficient new gridding algorithm using singular value decomposition. Magn Reson Med. 1998; 40(1):14–23. [PubMed: 9660548]
28. Fessler, J. Image reconstruction toolbox. http://web.eecs.umich.edu/~fessler/code/index.html
29. Rasche V, Proksa R, Sinkus R, Börnert P, Eggers H. Resampling of data between arbitrary grids using convolution interpolation. IEEE Trans Med Imaging. 1999; 18(5):385–92. [PubMed: 10416800]
30. De Zanche N, Barmet C, Nordmeyer-Massner Ja, Pruessmann KP. NMR probes for measuring magnetic fields and field dynamics in MR systems. Magn Reson Med. 2008; 60(1):176–86. [PubMed: 18581363]
31. Mason GF, Harshbarger T, Hetherington HP, Zhang Y, Pohost GM, Twieg DB. A method to measure arbitrary k-space trajectories for rapid MR imaging. Magn Reson Med. 1997; 38(3):492–6. [PubMed: 9339451]
32. Duyn JH, Yang Y, Frank JA, van der Veen JW. Simple correction method for k-space trajectory deviations in MRI. J Magn Reson. 1998; 132(1):150–3. [PubMed: 9615415]
33. Pipe JG. Reconstructing MR images from undersampled data: data-weighting considerations. Magn Reson Med. 2000; 43(6):867–75. [PubMed: 10861882]
34. Sodickson DK, Manning WJ. Simultaneous acquisition of spatial harmonics (SMASH): fast imaging with radiofrequency coil arrays. Magn Reson Med. 1997; 38(4):591–603. [PubMed: 9324327]

35. Pruessmann KP, Weiger M, Scheidegger MB, Boesiger P. SENSE: sensitivity encoding for fast MRI. Magn Reson Med. 1999; 42(5):952–62. [PubMed: 10542355]
36. Griswold MA, Jakob PM, Heidemann RM, Nittka M, Jellus V, Wang J, Kiefer B, Haase A. Generalized autocalibrating partially parallel acquisitions (GRAPPA). Magn Reson Med. 2002; 47(6):1202–1210. [PubMed: 12111967]
37. Blaimer M, Breuer F, Mueller M, Heidemann RM, Griswold Ma, Jakob PM. SMASH, SENSE, PILS, GRAPPA: how to choose the optimal method. Top Magn Reson Imaging. 2004; 15(4):223–36. [PubMed: 15548953]
38. Deshmane A, Gulani V, Griswold MA, Seiberlich N. Parallel MR imaging. J Magn Reson Imaging. 2012; 36(1):55–72. [PubMed: 22696125]
39. Pruessmann KP. Encoding and reconstruction in parallel MRI. NMR Biomed. 2006; 19(3):288–99. [PubMed: 16705635]
40. Breuer FA, Kannengiesser SAR, Blaimer M, Seiberlich N, Jakob PM, Griswold MA. General formulation for quantitative G-factor calculation in GRAPPA reconstructions. Magn Reson Med. 2009; 62(3):739–46. [PubMed: 19585608]
41. Seiberlich N, Breuer F, Heidemann R, Blaimer M, Griswold M, Jakob P. Reconstruction of undersampled non-Cartesian data sets using pseudo-Cartesian GRAPPA in conjunction with GROG. Magn Reson Med. 2008; 59(5):1127–37. [PubMed: 18429026]
42. Heberlein K, Hu X. Auto-calibrated parallel spiral imaging. Magn Reson Med. 2006; 55(3):619–25. [PubMed: 16453323]
43. Griswold MA, Jakob PM, Nittka M, Goldfarb JW, Haase A. Partially parallel imaging with localized sensitivities (PILS). Magn Reson Med. 2000; 44(4):602–609. [PubMed: 11025516]
44. Eggers, H.; Boernert, P.; Boesiger, P. Proc of the 9th Annual Meeting of the Int Soc Magn Reson Med. Vol. 9. Glasgow: 2001. Real-Time Partial Parallel Spiral Imaging with Localized Sensitivities; p. 1772
45. Liu C, Bammer R, Moseley ME. Parallel imaging reconstruction for arbitrary trajectories using k-space sparse matrices (kSPA). Magn Reson Med. 2007; 58(6):1171–81. [PubMed: 17969012]
46. Yeh EN, McKenzie CA, Ohliger MA, Sodickson DK. Parallel magnetic resonance imaging with adaptive radius in k-space (PARS): constrained image reconstruction using k-space locality in radiofrequency coil encoded data. Magn Reson Med. 2005; 53(6):1383–92. [PubMed: 15906283]
47. Samsonov AA, Block WF, Arunachalam A, Field AS. Advances in locally constrained k-space-based parallel MRI. Magn Reson Med. 2006; 55(2):431–8. [PubMed: 16369917]
48. Hu, P.; Meyer, C. Proc of the 14th Annual Meeting of the Int Soc Magn Reson Med. Vol. 6. Seattle: 2006. BOSCO: Parallel Image Reconstruction Based on Successive Convolution Operations; p. 10
49. Kannengießer, SAR.; Brenner, AR.; Noll, TG. Accelerated Image Reconstruction for Sensitivity Encoded Imaging with Arbitrary k – Space Trajectories; Proc of the 8th Annual Meeting of the Int Soc Magn Reson Med; Denver. 2000; p. 155
50. Hestenes M, Stiefel E. Methods of conjugate gradients for solving linear systems. J Res Natl Bur Stand (1934). 1952; 49(6):409–436.
51. Wajer, F.; Pruessmann, KP. Proc of the 9th Annual Meeting of the Int Soc Magn Reson Med. Vol. 9. Glasgow: 2001. Major Speedup of Reconstruction for Sensitivity Encoding with Arbitrary Trajectories; p. 767
52. Qu P, Zhong K, Zhang B, Wang J, Shen GX. Convergence behavior of iterative SENSE reconstruction with non-Cartesian trajectories. Magn Reson Med. 2005; 54(4):1040–5. [PubMed: 16149063]
53. Lin FH, Kwong KK, Belliveau JW, Wald LL. Parallel imaging reconstruction using automatic regularization. Magn Reson Med. 2004; 51(3):559–67. [PubMed: 15004798]
54. Liu B, King K, Steckner M, Xie J, Sheng J, Ying L. Regularized sensitivity encoding (SENSE) reconstruction using Bregman iterations. Magn Reson Med. 2009; 61(1):145–52. [PubMed: 19097223]
55. Bydder M, Perthen JE, Du J. Optimization of sensitivity encoding with arbitrary k-space trajectories. Magn Reson Imaging. 2007; 25(8):1123–9. [PubMed: 17905244]

56. Ying, L.; Xu, D.; Liang, ZP. Proc of the 26th Annual Int Conference of the IEEE EMBS. Vol. 2. San Francisco: 2004. On Tikhonov regularization for image reconstruction in parallel MRI; p. 1056-9.
57. Tikhonov, AN.; Arsenin, VI. Solutions of ill-posed problems. Washington/New York: Winston, distributed by Halsted Press; 1977.
58. Block KT, Uecker M, Frahm J. Undersampled radial MRI with multiple coils. Iterative image reconstruction using a total variation constraint. Magn Reson Med. 2007; 57(6):1086–98. [PubMed: 17534903]
59. Rudin L, Osher S, Fatemi E. Nonlinear total variation based noise removal algorithms. Phys D Nonlinear Phenom. 1992; 60:259–268.
60. Lustig M, Donoho D, Pauly JM. Sparse MRI: The application of compressed sensing for rapid MR imaging. Magn Reson Med. 2007; 58(6):1182–95. [PubMed: 17969013]
61. Hansen MS, Sørensen TS. Gadgetron: an open source framework for medical image reconstruction. Magn Reson Med. 2013; 69(6):1768–76. [PubMed: 22791598]
62. Hansen, M. Nuts & Bolts of Advanced Imaging: Image Reconstruction – Parallel Imaging. Proc of the 21st Annual Meeting of the Int Soc Magn Reson Med. 2013. http://gadgetron.sourceforge.net/sunrise/
63. Walsh D, Gmitro A, Marcellin M. Adaptive reconstruction of phased array MR imagery. Magn Reson Med. 2000; 43(5):682–90. [PubMed: 10800033]
64. Weiger M, Pruessmann KP, Osterbauer R, Börnert P, Boesiger P, Jezzard P. Sensitivity-encoded single-shot spiral imaging for reduced susceptibility artifacts in BOLD fMRI. Magn Reson Med. 2002; 48(5):860–6. [PubMed: 12418001]
65. Sussman MS, Stainsby Ja, Robert N, Merchant N, Wright Ga. Variable-density adaptive imaging for high-resolution coronary artery MRI. Magn Reson Med. 2002; 48(5):753–64. [PubMed: 12417989]
66. Hansen MS, Atkinson D, Sorensen TS. Cartesian SENSE and k-t SENSE reconstruction using commodity graphics hardware. Magn Reson Med. 2008; 59(3):463–8. [PubMed: 18306398]
67. Liu, B.; Yi Ming, Zou; Leslie, Ying. Sparsesense: Application of compressed sensing in parallel MRI; 2008 International Conference on Technology and Applications in Biomedicine; Shenzhen, China. IEEE; 2008. p. 127-130.
68. Otazo R, Kim D, Axel L, Sodickson DK. Combination of compressed sensing and parallel imaging for highly accelerated first-pass cardiac perfusion MRI. Magn Reson Med. 2010; 64(3):767–76. [PubMed: 20535813]
69. Shin T, Nayak KS, Santos JM, Nishimura DG, Hu BS, McConnell MV. Three-dimensional first-pass myocardial perfusion MRI using a stack-of-spirals acquisition. Magn Reson Med. 2013; 69(3):839–44. [PubMed: 22556062]
70. Heberlein K, Kadah Y, Hu X. Segmented spiral parallel imaging using GRAPPA. Proc of the 11th Annual Meeting of the Int Soc Magn Reson Med. 2004:328.
71. Heidemann RM, Griswold MA, Seiberlich N, Nittka M, Kannengiesser SAR, Kiefer B, Jakob PM. Fast method for 1D non-cartesian parallel imaging using GRAPPA. Magn Reson Med. 2007; 57(6):1037–46. [PubMed: 17534925]
72. Breuer FA, Moriguchi H, Seiberlich N, Blaimer M, Jakob PM, Duerk JL, Griswold MA. Zigzag sampling for improved parallel imaging. Magn Reson Med. 2008; 60(2):474–8. [PubMed: 18666134]
73. Skare S, Newbould RD, Nordell A, Holdsworth SJ, Bammer R. An auto-calibrated, angularly continuous, two-dimensional GRAPPA kernel for propeller trajectories. Magn Reson Med. 2008; 60(6):1457–65. [PubMed: 19025911]
74. Saybasili H, Herzka DA, Barkauskas K, Seiberlich N, Griswold MA. Multi-Node, Multi-GPU Radial GRAPPA Reconstruction for Online, Real-Time, Low-Latency MRI. Proc of the 21st Annual Meeting of the Int Soc Magn Reson Med. 2013:185.
75. Breuer F, Kellman P. Dynamic autocalibrated parallel imaging using temporal GRAPPA (TGRAPPA). Magn Reson Med. 2005; 53(4):981–985. [PubMed: 15799044]

76. Ding Y, Chung Y, Jekic M, Simonetti O. A New Approach to Autocalibrated Dynamic Parallel Imaging Based on the Karhunen-Loeve Transform: KL-TSENSE and KL-TGRAPPA. Magn Reson Med. 2011; 65(6):1786–1792. [PubMed: 21254210]
77. Arunachalam A, Samsonov A, Block WF. Self-calibrated GRAPPA method for 2D and 3D radial data. Magn Reson Med. 2007; 57(5):931–8. [PubMed: 17457884]
78. Codella NCF, Spincemaille P, Prince M, Wang Y. A radial self-calibrated (RASCAL) generalized autocalibrating partially parallel acquisition (GRAPPA) method using weight interpolation. NMR Biomed. 2011; 24(7):844–54. [PubMed: 21834008]
79. Breuer FA, Blaimer M, Mueller MF, Seiberlich N, Heidemann RM, Griswold MA, Jakob PM. Controlled aliasing in volumetric parallel imaging (2D CAIPIRINHA). Magn Reson Med. 2006; 55(3):549–56. [PubMed: 16408271]
80. Yutzy SR, Seiberlich N, Duerk JL, Griswold MA. Improvements in multislice parallel imaging using radial CAIPIRINHA. Magn Reson Med. 2011; 65(6):1630–7. [PubMed: 21287592]
81. Lustig, M.; Alley, M.; Vasanawala, S.; Donoho, D.; Pauly, JM. L1 SPIR-iT : Autocalibrating Parallel Imaging Compressed Sensing; Proc of the 17th Annual Meeting of the Int Soc Magn Reson Med; Honolulu. 2009; p. 334
82. Murphy M, Alley M, Demmel J, Keutzer K, Vasanawala S, Lustig M. Fast l1-SPIRiT compressed sensing parallel imaging MRI: scalable parallel implementation and clinically feasible runtime. IEEE Trans Med Imaging. 2012; 31(6):1250–62. [PubMed: 22345529]
83. Lai, P.; Lustig, M.; Brau, A.; Vasanawala, S.; Beatty, P.; Alley, M. Efficient L1SPIRiT Reconstruction (ESPIRiT) for Highly Accelerated 3D Volumetric MRI with Parallel Imaging and Compressed Sensing; Proc of the 18th Annual Meeting of the Int Soc Magn Reson Med; Stockholm, Sweden. 2010; p. 345
84. Jeong HJ, Eddleman CS, Shah S, Seiberlich N, Griswold Ma, Batjer HH, Carr JC, Carroll TJ. Accelerating time-resolved MRA with multiecho acquisition. Magn Reson Med. 2010; 63(6): 1520–8. [PubMed: 20512855]
85. Cashen T, Carroll T. Hybrid Radial-Parallel 3D Imaging. Proc of the 13th Annual Meeting of the Int Soc Magn Reson Med. 2005; 13:288.
86. Kressler B, Spincemaille P, Nguyen TD, Cheng L, Xi Hai Z, Prince MR, Wang Y. Three-dimensional cine imaging using variable-density spiral trajectories and SSFP with application to coronary artery angiography. Magn Reson Med. 2007; 58(3):535–43. [PubMed: 17763360]
87. Haider C, Glockner J, Stanson A, Riederer SJ. Peripheral Vasculature: High-Temporal-and High-Spatial-Resolution Three-dimensional Contrast-enhanced MR Angiography1. Radiology. 2009; 253(3):831–843. [PubMed: 19789238]
88. Haider CR, Borisch Ea, Glockner JF, Mostardi PM, Rossman PJ, Young PM, Riederer SJ. Max CAPR: high-resolution 3D contrast-enhanced MR angiography with acquisition times under 5 seconds. Magn Reson Med. 2010; 64(4):1171–81. [PubMed: 20715291]
89. Trzasko JD, Haider CR, Borisch Ea, Campeau NG, Glockner JF, Riederer SJ, Manduca A. Sparse-CAPR: highly accelerated 4D CE-MRA with parallel imaging and nonconvex compressive sensing. Magn Reson Med. 2011; 66(4):1019–32. [PubMed: 21608028]
90. Mostardi PM, Young PM, McKusick Ma, Riederer SJ. High temporal and spatial resolution imaging of peripheral vascular malformations. J Magn Reson Imaging. 2012; 36(4):933–42. [PubMed: 22674646]
91. Xu J, Kim D, Otazo R, Srichai MB, Lim RP, Axel L, McGorty KA, Niendorf T, Sodickson DK. Towards a five-minute comprehensive cardiac MR examination using highly accelerated parallel imaging with a 32-element coil array: Feasibility and initial comparative evaluation. J Magn Reson Imaging. 2013; 38(1):180–8. [PubMed: 23197471]
92. Saybasili H, Herzka D, Seiberlich N, Griswold M. Low-Latency Radial GRAPPA Reconstruction using Multi-Core CPUs and General Purpose GPU Programming. Proc of the 20th Annual Meeting of the Int Soc Magn Reson Med. 2012; 20:2554.
93. Hansen MS, Baltes C, Tsao J, Kozerke S, Pruessmann KP, Eggers H. k-t BLAST reconstruction from non-Cartesian k-t space sampling. Magn Reson Med. 2006; 55(1):85–91. [PubMed: 16323167]

94. Hansen MS, Sørensen TS, Arai AE, Kellman P. Retrospective reconstruction of high temporal resolution cine images from real-time MRI using iterative motion correction. Magn Reson Med. 2012; 68(3):741–50. [PubMed: 22190255]

95. Kolbitsch C, Prieto C, Buerger C, Harrison J, Razavi R, Smink J, Schaeffter T. Prospective high-resolution respiratory-resolved whole-heart MRI for image-guided cardiovascular interventions. Magn Reson Med. 2012; 68(1):205–13. [PubMed: 22183798]

96. Tsao J, Kozerke S, Boesiger P, Pruessmann KP. Optimizing spatiotemporal sampling for k-t BLAST and k-t SENSE: application to high-resolution real-time cardiac steady-state free precession. Magn Reson Med. 2005; 53(6):1372–82. [PubMed: 15906282]

97. Xie J, Lai P, Huang F, Li Y, Li D. Cardiac magnetic resonance imaging using radial k-space sampling and self-calibrated partial parallel reconstruction. Magn Reson Imaging. 2010; 28(4): 495–506. [PubMed: 20061114]

98. Yeh EN, Stuber M, McKenzie Ca, Botnar RM, Leiner T, Ohliger Ma, Grant AK, Willig-Onwuachi JD, Sodickson DK. Inherently self-calibrating non-Cartesian parallel imaging. Magn Reson Med. 2005; 54(1):1–8. [PubMed: 15968671]

99. Huang F, Lin W, Duensing GR, Reykowski A. K-t sparse GROWL: sequential combination of partially parallel imaging and compressed sensing in k-t space using flexible virtual coil. Magn Reson Med. 2012; 68(3):772–82. [PubMed: 22162191]

100. Feng L, Srichai MB, Lim RP, Harrison A, King W, Adluru G, Dibella EVR, Sodickson DK, Otazo R, Kim D. Highly accelerated real-time cardiac cine MRI using k-t SPARSE-SENSE. Magn Reson Med. 2012; 74:64–74. [PubMed: 22887290]

101. Kwon KT, Wu HH, Shin T, Çukur T, Lustig M, Nishimura DG. Three-dimensional magnetization-prepared imaging using a concentric cylinders trajectory. Magn Reson Med. 2013; 000(April):n/a–n/a.

102. Bi X, Park J, Larson AC, Zhang Q, Simonetti O, Li D. Contrast-enhanced 4D radial coronary artery imaging at 3.0 T within a single breath-hold. Magn Reson Med. 2005; 54(2):470–5. [PubMed: 16032681]

103. Prieto C, Uribe S, Razavi R, Atkinson D, Schaeffter T. 3D undersampled golden-radial phase encoding for DCE-MRA using inherently regularized iterative SENSE. Magn Reson Med. 2010; 64(2):514–26. [PubMed: 20665795]

104. Glover GH, Law CS. Spiral-in/out BOLD fMRI for increased SNR and reduced susceptibility artifacts. Magn Reson Med. 2001; 46(3):515–22. [PubMed: 11550244]

105. Assländer J, Zahneisen B, Hugger T, Reisert M, Lee HL, LeVan P, Hennig J. Single shot whole brain imaging using spherical stack of spirals trajectories. Neuroimage. 2013; 73:59–70. [PubMed: 23384526]

106. Perthen JE, Bydder M, Restom K, Liu TT. SNR and functional sensitivity of BOLD and perfusion-based fMRI using arterial spin labeling with spiral SENSE at 3 T. Magn Reson Imaging. 2008; 26(4):513–22. [PubMed: 18158226]

107. Lebel RM, Jones J, Ferre JC, Law M, Nayak KS. Highly accelerated dynamic contrast enhanced imaging. Magn Reson Med. 2013; 000:1–10.

108. Brodsky EK, Bultman EM, Johnson KM, Horng DE, Schelman WR, Block WF, Reeder SB. High-spatial and high-temporal resolution dynamic contrast-enhanced perfusion imaging of the liver with time-resolved three-dimensional radial MRI. Magn Reson Med. 2013; 000

109. Chandarana H, Feng L, Block TK, Rosenkrantz AB, Lim RP, Babb JS, Sodickson DK, Otazo R. Free-breathing contrast-enhanced multiphase MRI of the liver using a combination of compressed sensing, parallel imaging, and golden-angle radial sampling. Invest Radiol. 2013; 48(1):10–6. [PubMed: 23192165]

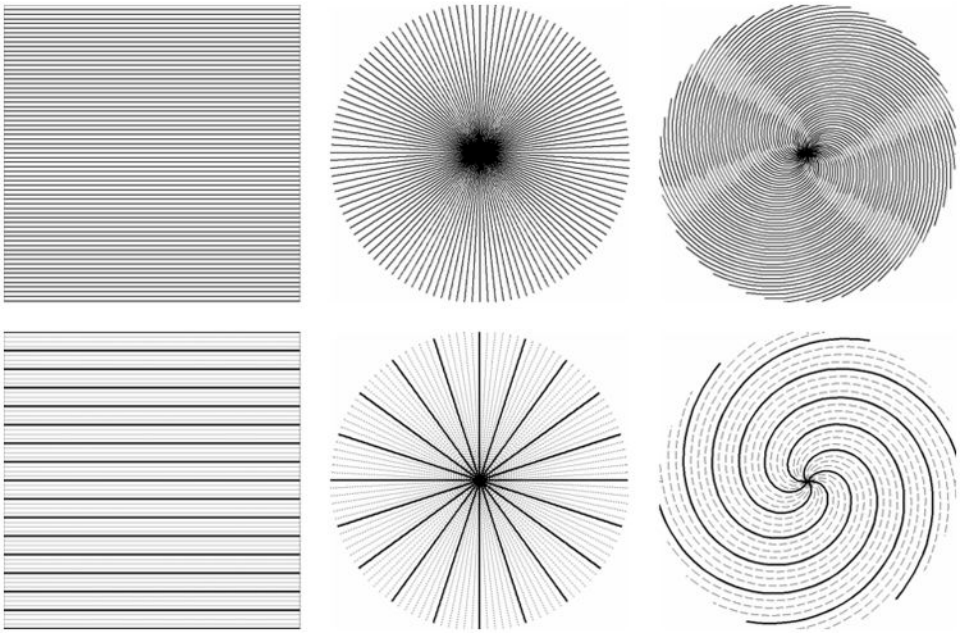

Figure 1.
Fully-sampled (top row) and undersampled (bottom row) Cartesian, radial, and spiral trajectories.

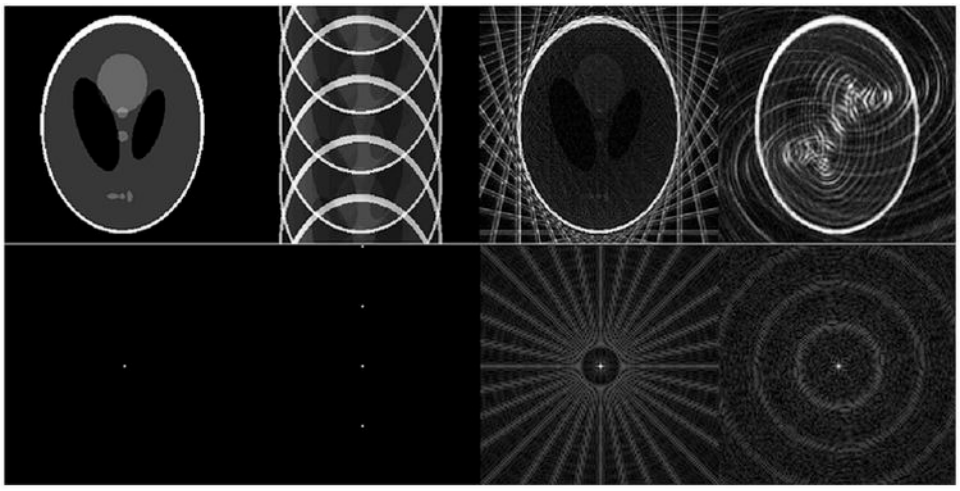

Figure 2.

Characteristic undersampling artifacts (top) and point spread functions (bottom) for several non-Cartesian trajectories. The fully-sampled reference image and its point spread function are shown on the far left. The other images show artifacts from an undersampled Cartesian trajectory and its PSF (middle left), undersampled radial trajectory (middle right), and undersampled variable density spiral trajectory (far right).

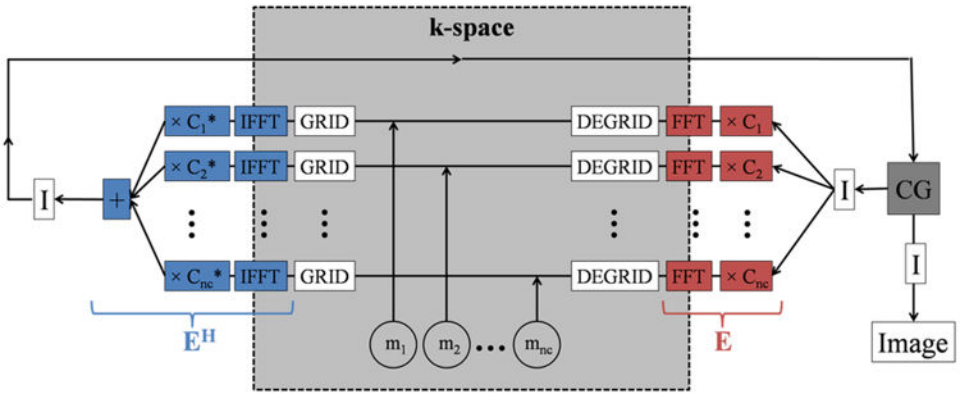

Figure 3.

A summary of the CG SENSE algorithm, which reconstructs an image from undersampled non-Cartesian data. Undersampled, multi-channel k-space data (m_1, m_2,…,m_{nc}) are acquired and fed into the algorithm. These data are density compensated, gridded, the inverse Fourier transform calculated, and the multi-coil images are multiplied by the conjugate of the coil sensitivities. The multi-coil images are summed and intensity corrected to produce a single image, which is fed into the CG algorithm. The CG algorithm finds a new estimate for the reconstructed image. If the reconstruction has not converged, intensity correction is applied, the image is multiplied by the coil sensitivities, the Fourier transform is calculated, the data are degridded, the original data replaced, and the next iteration begins. This process continues until the reconstruction converges and a stopping criterion has been met. Once the stopping criteria are met, intensity correction is applied, and the result is an unaliased image.

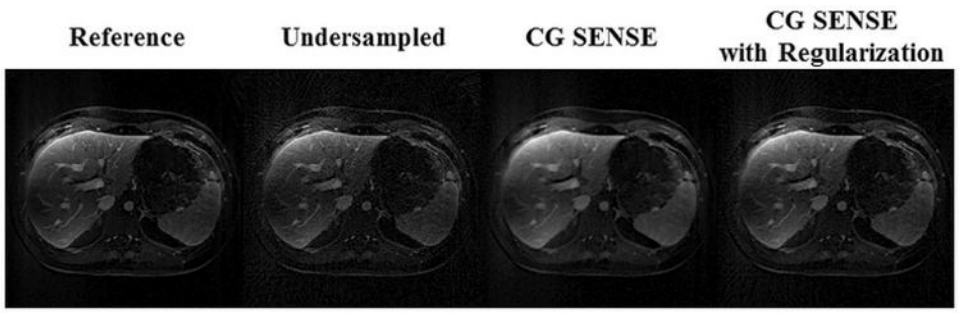

Figure 4.

Left: Fully-sampled breathhold abdominal image generated using 200 projections. Center-left: Reconstructed data retrospectively undersampled by a radial acceleration factor of 4 (50 projections) and gridded using NUFFT. Center-right: The corresponding CG SENSE reconstruction. Right: The corresponding CG SENSE reconstruction with Tikhonov regularization.

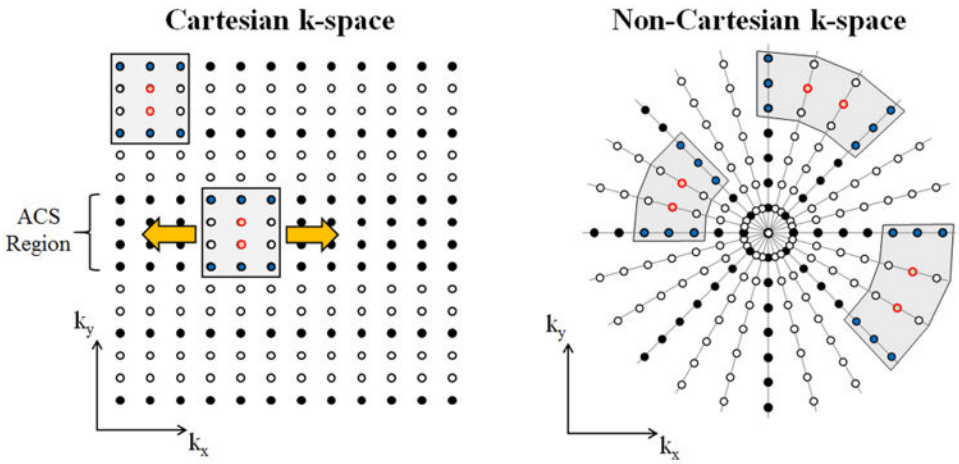

Figure 5.

Left: Cartesian data undersampled by a factor of R=3, where with acquired data points as filled black circles and missing points as white circles. An example 2×3 Cartesian GRAPPA kernel is shown where source points are illustrated as filled blue circles, and target points as empty circles outlined in red. Note that by collecting kernel repetitions in the fully-sampled center patch of Cartesian k-space (the ACS region), the GRAPPA weights for this arrangement of source and target points can be determined. Right: Radial k-space with an acceleration factor of R=3. Three different 2×3 non-Cartesian GRAPPA kernels are shown; note that the direction and distance between source and target points changes for each of the kernels, so each kernel requires a unique set of non-Cartesian GRAPPA weights.

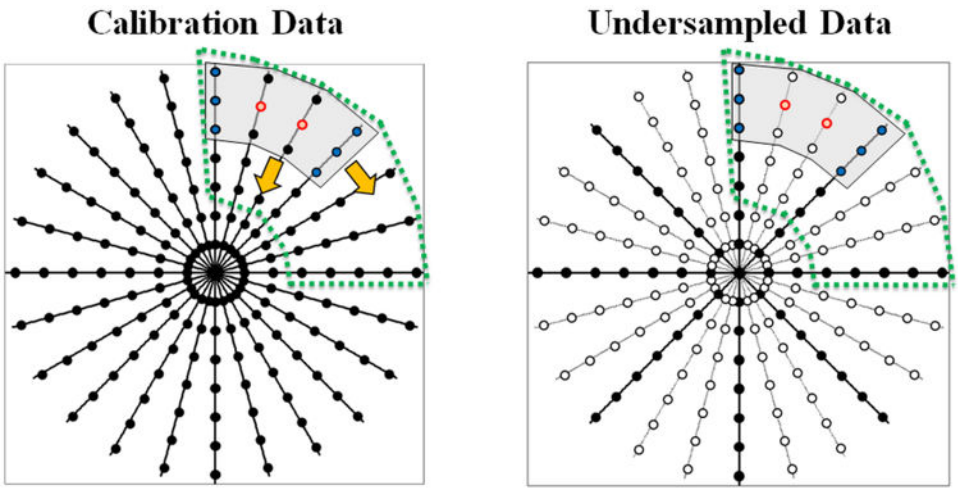

Figure 6.

A fully-sampled radial k-space and an example segment which can be used to find the GRAPPA weights for the specific kernel shape shown. Note that by sliding the kernel through the segment (bottom left), a total of 12 kernel repetitions can be found for calibration. (Right) The undersampled radial k-space, with the source and target points corresponding to the GRAPPA kernel on the left-hand side of the figure. The data within this segment can be reconstructed using the GRAPPA weights from the calibration segment shown at left.

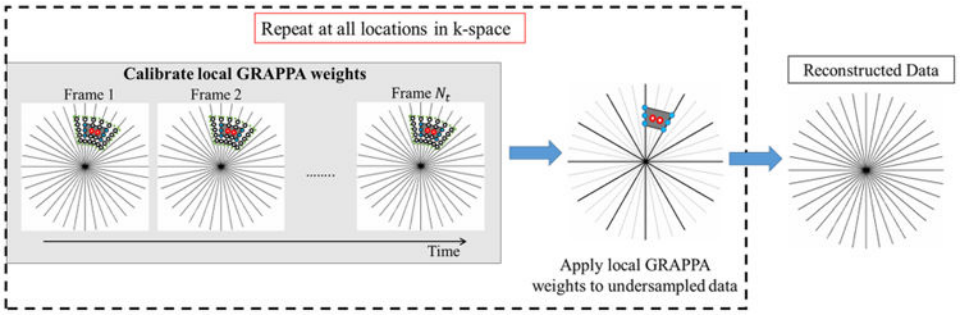

Figure 7.

A schematic of the non-Cartesian GRAPPA reconstruction. First, one or several fully-sampled datasets are acquired for calibration. The weights for each geometry can be determined using either k-space segmentation, through-time calibration, or a combination of the two. These weights are applied to the undersampled data at the appropriate location to reconstruct each target point. This process is repeated for each arrangement of source and target points to recover the fully-sampled k-space.

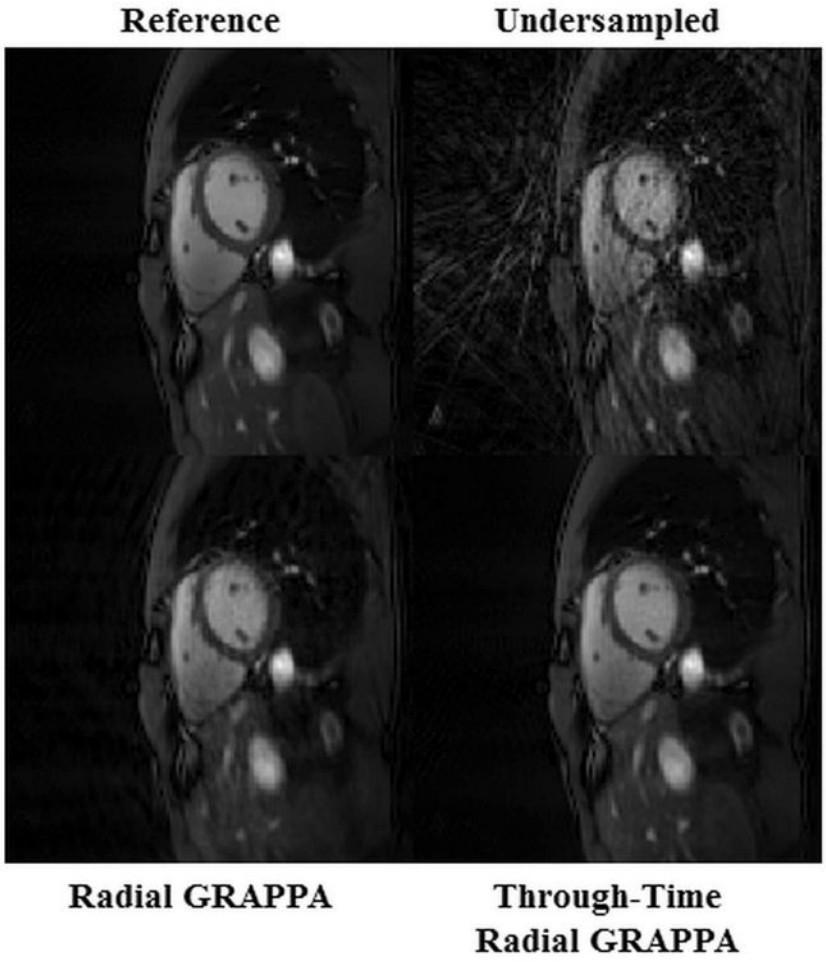

Figure 8.

Representative cardiac images from a non-gated, free-breathing cardiac scan. Data were acquired with grid size 128×128 and 144 projections, and were retrospectively undersampled to 16 projections(acceleration factor R=12.6 with respect to the Nyquist limit). The fully-sampled image (top left) is shown along with the following reconstruction methods: (top right) direct gridding of undersampled data, (bottom left) radial GRAPPA with a k-space segment spanning 64 readout points and 10 projections, and (bottom right) through-time radial GRAPPA calibrated with 20 frames and a k-space segment spanning 8 readout points and 4 projections.

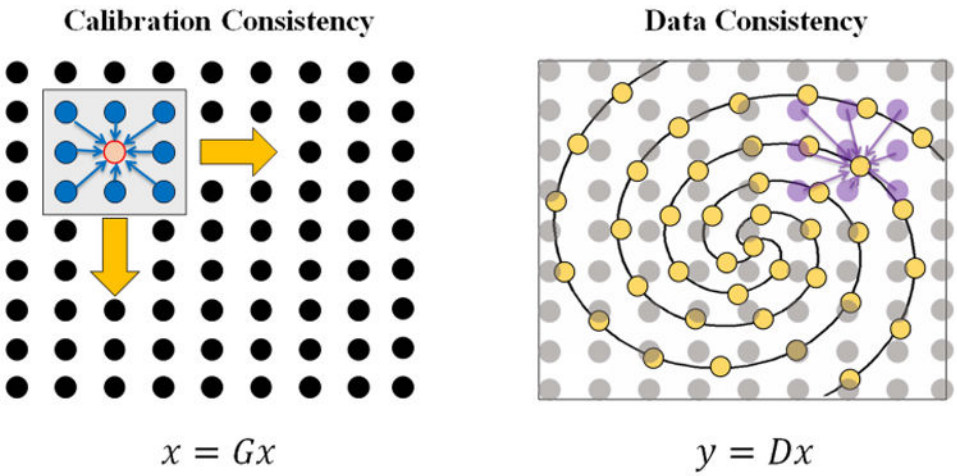

Figure 9.

Left: The SPIRiT kernel enforces calibration consistency. A 3×3 SPIRiT kernel is depicted which is successively applied to every data point in the synthesized Cartesian k-space. At a given k-space location, the value of the target point, outlined in red, is known for the current iteration. The SPIRiT kernel multiplies source points, shown as filled blue circles, by a set of coefficients and sums the results to yield an estimate of the target point. The iterative process is terminated when the actual and estimated values are equal (within a specified error metric). Right: Data consistency is evaluated by transforming the reconstructed Cartesian data points back onto the undersampled non-Cartesian trajectory. Nearby points from the synthesized Cartesian k-space (shown in purple) are used to interpolate the value of a given point on the undersampled non-Cartesian trajectory, as indicated by the arrows. If the result of this operation agrees with the data that was originally collected, then the reconstruction is said to be consistent with the acquired data.

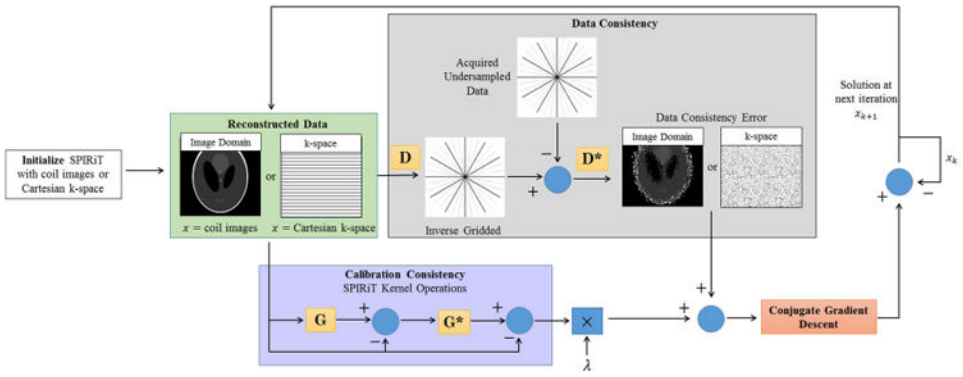

Figure 10.

A flowchart for SPIRiT reconstruction. Reconstruction can be performed using either a k-space domain or image domain approach, and both techniques are depicted. The first step is to initialize the algorithm with an estimate of *x*, which is either a Cartesian k-space or uncombined coil images. Next, the operator *D* samples *x* along points on the undersampled non-Cartesian trajectory. The difference between this result and the original undersampled data is called the data consistency error. Calibration consistency is assessed using the operator *G*, which convolves the reconstructed Cartesian k-space with the SPIRiT kernel (k-space domain approach) or multiplies the reconstructed coil images by the inverse FFT of the SPIRiT kernel (image domain approach). The derivative of the objective function, shown in Eq. 19, is computed as a sum involving both calibration consistency and data consistency terms, and conjugate gradient descent returns an improved estimate of the reconstructed Cartesian k-space or coil images for the next iteration. The algorithm terminates when a suitable stopping criterion is met.

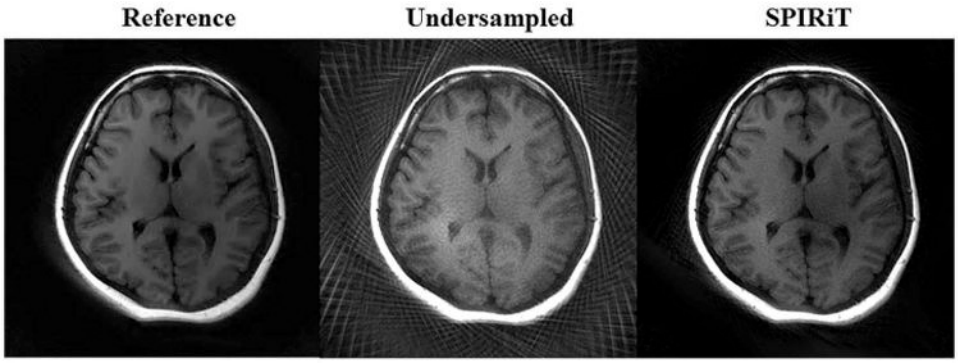

Figure 11.

Left: Fully-sampled images are shown for a T1-weighted BLADE acquisition with 44 blades and 9 lines per blade. Center: These data were retrospectively undersampled such that 44 blades with 3 lines per blade were used and are shown after a gridding reconstruction to demonstrate the amount of aliasing artifacts. Right: The corresponding SPIRiT reconstruction.

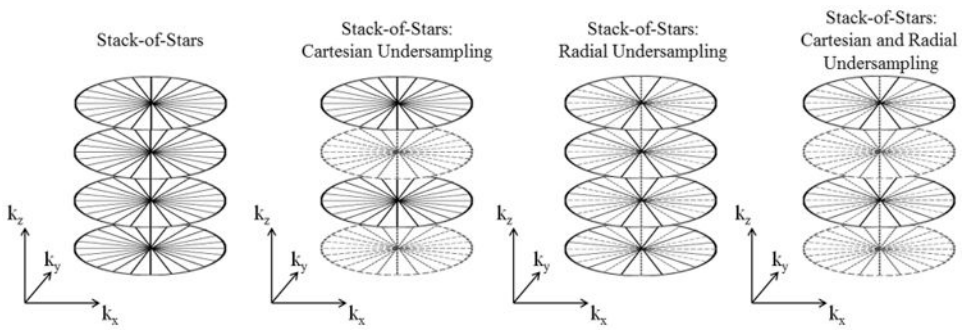

Figure 12.

Left: Fully-sampled, 3D stack-of-stars trajectory. These trajectories use a non-Cartesian trajectory in k_x-k_y plane and Cartesian encoding along k_z. Center Left: Stack-of-stars trajectory with Cartesian undersampling, where some k_z encoding lines are skipped. Center Right: Stack-of-stars trajectory with radial undersampling, where some projections are skipped. Right: Stack-of-stars trajectory with Cartesian and radial undersampling, where some k_z encoding lines and some projections are skipped.

Table 1

Summary of non-Cartesian parallel imaging methods implemented in this review.

Method Name	Manuscript Title(s)	Authors	Year	Image Domain or k-Space	Iterative or Direct	Calibration Data	Sampling Schemes
CG SENSE	SENSE with Arbitrary k-Space Trajectories	Pruessmann, KP, et al.	2001	Image Domain	Iterative	Coil Maps	Arbitrary
Non-Cartesian GRAPPA	Direct Parallel Imaging Reconstruction of Radially Sampled Data using GRAPPA with Relative Shifts.	Griswold, MA, et al.	2003	k-Space	Direct	ACS	Radial
	Auto-Calibrated Parallel Spiral Imaging.	Heberlein, K., Hu, X.	2006	k-Space	Direct	ACS	Spiral
	Direct Parallel Image Reconstructions for Spiral Trajectories using GRAPPA.	Heidemann, R, et al.	2006	k-Space	Direct	ACS	Spiral
	Improved Radial GRAPPA Calibration for Real-Time Free-Breathing Cardiac Imaging	Seiberlich, N, et al.	2011	k-Space	Direct	ACS	Radial
	Improved Temporal Resolution in Cardiac Imaging using Through-Time Spiral GRAPPA	Seiberlich, N, et al.	2011	k-Space	Direct	ACS	Spiral
SPIRiT	SPIRiT: Iterative Self-consistent Parallel Imaging Reconstruction from Arbitrary k-Space	Lustig, M., Pauly, JM.	2010	Image domain or k-Space	Iterative	Self-calibrating or Cartesian ACS	Arbitrary